Sensitivity of voxel-based estimations of leaf area density with terrestrial LiDAR to vegetation structure and sampling limitations: A simulation experiment

Maxime Soma, François Pimont, Jean-Luc Dupuy

HAL Id: hal-03353461

https://hal.inrae.fr/hal-03353461v1

Submitted on 9 Mar 2023

1   **Sensitivity of voxel-based estimations of Leaf Area Density with Terrestrial LiDAR to vegetation**

2   **structure and sampling limitations: a simulation experiment**

3   Maxime Soma[1,2*], François Pimont[1], Jean-Luc Dupuy[1]

4   [1] UR 629 Ecologie des Forêts Méditerranéennes (URFM), INRAe, 84914 Avignon, France

5   [2] UMR 114 EMMAH, UMT CAPTE, INRAe, 84914 Avignon, France

6   **Abstract**

7   The need for fine scale description of vegetation structure is increasing as Leaf Area Density

8   (LAD, m^2/m^3) becomes a critical parameter to understand ecosystem functioning and energy

9   and mass fluxes in heterogeneous ecosystems. Terrestrial Laser Scanning (TLS) has shown

10   great potential for retrieving the foliage area at stand, plant or voxel scales. Several sources of

11   measurement errors have been identified and corrected over the past years. However,

12   measurements remain sensitive to several factors, including, 1) voxel size and vegetation

13   structure within voxels, 2) heterogeneity in sampling from TLS instrument (occlusion and

14   shooting pattern), the consequences of which have been seldom analyzed at the scale of forest

15   plots. In the present paper, we aimed at disentangling biases and errors in plot-scale

16   measurements of LAD with TLS in a simulated vegetation scene. Two negative biases were

17   formerly attributed to (i) the unsampled voxels and to (ii) the subgrid vegetation heterogeneity

18   (i.e. clumping effect), and then quantified, thanks to a the simulation experiment providing

19   known LAD references at voxel scale, vegetation manipulations and unbiased point

20   estimators. We used confidence intervals to evaluate voxel-scale measurement accuracy.

21   We found that the unsampled voxel effect (i) led to underestimations with the "mean layer"

22   method –commonly used to fill unsampled voxels- for small voxels (0.1-0.2 m) and/or low

23   number of scans (<4). It was explained by the spatial correlations in vegetation, which

24   induced that dense voxels were more often occluded by dense neighbors than light voxels.

25   The distribution of the bias was heterogeneous in canopy, the bias being stronger at mid

canopy where occlusion started, but smaller in highly-occluded upper layers. This somehow counterintuitive result was explained by a more random sampling of upper layers, but could highly depend on vegetation structure.

The subgrid vegetation heterogeneity effect (ii) was confirmed to increase with voxel size, yet, the magnitude of this bias -quantified with vegetation manipulation- was found to be more homogeneously-distributed than the unsampled voxel effect.

Overall, we found that no scenario was unbiased. However, an intermediate voxel size (0.5m) was the best option, because the relatively homogeneous subgrid effect could be handled with a single correction factor and voxel-scale measurements errors were reasonable. On the contrary, smaller voxels led to poor voxel-scale measurements and variable biases in magnitude and spatial distribution with sampling design. However, more similar research in other context is required to adapt these conclusions to other forest plots.

1.   Introduction

The tridimensional distribution of vegetation in forest ecosystems constitutes a complex

surface of exchange between canopies, ground and atmosphere, driving mass and energy fluxes

(Norman and Campbell, 1989). Characterizing its structure is key for monitoring health and carbon

storage of forests, but also for understanding and modelling tree ecophysiological processes. This

amount of vegetation can be described by the Leaf Area Density (LAD) distribution, i.e. the total leaf

area per unit of volume (Weiss et al., 2004). In the past decade, LiDAR technologies have been used

for measuring LAD at various scales. Airborne LiDAR can provide canopy profile estimates at coarse

grains and over large areas, which is very useful for forests monitoring, but estimates can hardly be

evaluated against ground references (Kamoske et al., 2019; Stark et al., 2012). Meanwhile, Terrestrial

laser scanning (TLS) has been used successfully for local measuring, such as the total leaf area of

individual trees (Béland et al., 2011; Hosoi et al., 2010; Hu et al., 2018) and the LAD profiles at plot

scale (Pimont et al., 2016; Schneider et al., 2019). The detailed 3D point clouds provided by TLS can

closely describe the scene in three dimensions, the density of points being related to the presence of

vegetation (Durrieu et al., 2008). LAD or PAD (Plant Area Density, i.e. vegetation area density,

indiscriminate between leaf and wood material) has been estimated from a variety of methods based

on the similar theoretical background related to the attenuation of light in uniform medium. Typically,

most commonly used methods are inherited from Leaf Area Index measurements, and are based on the

Beer's law theory (Yan et al., 2019), i.e. the exponential attenuation of the transmittance along the

path of the beam, which readily relates the gap fraction and the attenuation coefficient of the medium.

Path length distribution models fully exploit the 3D information contained in point clouds by

accounting for the path length of beam within canopy before its interception, which has been shown to

provide better estimates (Yan et al., 2019), whether integrated to Beer's law approaches (Zhao et al.,

2015) or directly arising from contact frequency method (Béland et al., 2011; Pimont et al., 2019,

2018). LAD estimates can be retrieved either for a given layer in order to yield LAD profiles (Hosoi

and Omasa, 2006; Zhao et al., 2015) or directly within each voxel (Béland et al., 2011; Soma et al.,

2018). Measuring LAD at voxel scale is particularly relevant for optical measurements in non-uniform

77 canopies context because it allows to discriminate gaps and within crown volumes, thus limiting

78 clumping effect (Yan et al., 2019). Pimont et al. (2018) provided a detailed comparison of voxel-based

79 methods for the estimation of the attenuation coefficient within a single voxel, which is linearly

80 related to LAD/PAD. They introduced a more straightforward approach based on Maximum

81 Likelihood Estimation (MLE) and suggested corrections when the beam number was low and the

82 vegetation element size was not very small with respect to voxel size, resulting in an unbiased

83 estimator. In general, most theoretical estimates compare reasonably well with reference

84 measurements (Bailey and Mahaffee, 2017; Béland et al., 2011; Hu et al., 2018; Pimont et al., 2016;

85 Soma et al., 2018). However, TLS-based estimations are also affected by several biases, arising both

86 from inversion method and instrument limitations (Yan et al., 2019).

87   With the voxel-based approach, LiDAR estimates of LAD/PAD generally decrease with voxel

88 size (Bailey and Mahaffee, 2017; Béland et al., 2014a; Soma et al., 2018). Although the effect of voxel

89 size has been repeatedly observed (Cifuentes et al., 2014; Huang and Pretzsch, 2010; Li et al., 2016) ,

90 few studies conducted a complete analysis of this effect (Béland et al., 2014a; Grau et al., 2017). Such

91 an effect has been attributed to vegetation clumping, which induces the presence of heterogeneities in

92 the vegetation structure inside the voxel, referred to as subgrid vegetation heterogeneity. The choice of

93 too large voxels regarding vegetation structure hampers a proper discretization of gaps and clumps,

94 leading to a negative bias in estimates as a consequence of Jensen inequality (Ruel and Ayres, 1999).

95 Additionally, for some instruments, some critical overestimations of LAD occur as distance from

96 scanner increases. This bias has been attributed to the increase in effective footprint of the beam

97 associated with beam divergence (Soma et al. 2018). Both effects can be accounted for through an

98 adequate modelling of the LiDAR signal (Béland et al., 2014b, 2011) or simple calibration

99 coefficients (Soma et al. 2018). Such calibrations have been included in the unbiased estimator

100 approach presented in Pimont et al. (2019), in a new formulation of the estimation of the LAD, which

101 also includes a rigorous incorporation of the wood element volume and multiview LiDAR data

102 (Pimont et al. 2019).

103   Another important TLS drawback at plot scale, is the spatial variation in sampling quality

104 within point clouds (Schneider et al., 2019; Wilkes et al., 2017). Indeed, the geometry of the shooting

4

105 pattern of most TLS instruments (such as FARO 130X) has a fixed angular step resolution. Hence, the

106 beam density decreases with distance to scanner. The second source of variation in beam sampling is

107 vegetation occlusion: when a beam is fully intercepted (single hit for monoecho TLS or the last return

108 in case of multiecho TLS), it cannot explore beyond the intercepting voxel. This implies that fewer

109 beams remain when vegetation is present between the scanner and the voxel of interest. Both geometry

110 and occlusion contribute to the occurrence of unsampled voxels, where no information or limited

111 information is available. Since the reliability of LAD estimation within a given voxel strongly depends

112 on the number of beams exploring each voxel (Pimont et al., 2018), random errors in individual voxels

113 are very large when beam number is low. Some point estimators are theoretically unbiased (Pimont et

114 al., 2019, 2018), so that one could expect that the random errors will cancel when averaged over a

115 large number of voxels, e.g. when vertical profiles are computed.

116   This assumption, however, might not be correct in the field because of the presence of

117 unsampled voxels in the context of heterogeneous canopy. Indeed, one could expect that unsampled

118 voxels would mostly be located in dense vegetation spots, where occlusion is the strongest. At plot

119 scale, this could result in a sampling bias, leading to a potential underestimation of the mean LAD.

120 Typically, the most commonly used methods for correcting for occlusion relies on the mean estimate

121 in layers, i.e. on estimates within explored areas, which might not be representative of occluded areas

122 in clumped vegetation context. To date, few studies have conducted an analysis of occlusion

123 distribution, magnitude and mechanisms at tree (Béland et al., 2011; Yun et al., 2019) or plot scale

124 (Morsdorf et al., 2018; Schneider et al., 2019). Moreover, these studies did not formally disentangle

125 the relative contributions of unsampled voxels from subgrid vegetation heterogeneity, since both vary

126 with voxel size. Also, most previous studies carried out at tree or forest-plot scales relied on point

127 estimates with theoretical biases, which complicates the analysis of biases at tree or plot scales.

128   To improve sampling quality, a widespread practice during data acquisition is to acquire

129 multiple scans across the scene in order to increase both absolute number of beams and variety of

130 viewpoints (Côté et al., 2011; Wilkes et al., 2017). Moreover, the number of scans used in the field

131 and the scanner resolution are generally limited given technical constraints, such as time to proceed or

132 storage capability (Wilkes et al., 2017). This implies some constraints on voxel size used for

estimations, since the fraction of non-explored voxels strongly rises as voxel size decreases (Béland et

al., 2014a). Scanning design and post-processing recommendations accounting for these sampling

limitations are generally dedicated to applications such as detection of stems or measurement of tree

geometrical features (e.g. diameter) (Gollob et al., 2019; Wilkes et al., 2017), but recommendations

for description of canopies features are still rare at plot scale (Schneider et al., 2019).

Improving our understanding of the impacts of both heterogeneity effect and occlusion relying

on actual data is very challenging because of the lack of accuracy in references, particularly in dense

and complex canopy structure, while the estimation of leaf projection factor or leaf fraction are

additional sources of errors. In this difficult context, a simulation framework is mandatory to provide a

perfectly controlled environment to test various configurations and methods of estimations and

disentangle multiple sources of biases (Morsdorf et al., 2018; Yan et al., 2019), as done in Grau et al.,

(2017). In the present study, we rely on numerical experiments to analyze the sensitivity of LAD

estimations to biases arising from (1) vegetation heterogeneity and (2) heterogeneity of the sampling

quality at plot scale, which depends on both vegetation structure at canopy scale and sampling design.

We performed these simulations with unbiased point estimators in the framework of a Mediterranean

canopy sampled with a single echo terrestrial LiDAR. Here, we expect to disentangle and better

understand the mechanisms affecting estimations in the field, to analyze their magnitude and how they

distribute in forest plots, in order to finally derive recommendations on sampling design and selection

of appropriate voxel sizes.

2. **Numerical experiments**

2.1. Overview

The aim of the numerical experiments was to disentangle biases, errors and limitations arising

from voxel size and number of scans for the estimation of LAD in heterogeneous vegetation. For this,

we first generated a high resolution reference LAD field that had to meet the following requirements:

(i) it had to be as representative as possible of natural vegetation, with dense clumps (corresponding to

tree crowns) surrounded by empty locations (ii) it should be realistic for a forest plot, in terms of both

LAI and LAD profile, as occlusion patterns are highly sensitive to vegetation attenuation coefficient.

6

160   Generation of the LAD reference field (LAD_{REF}) is described in section 2.2. This field had a resolution

161   of 0.1 m. An additional smoother reference fields of the same vegetation scene ($LAD_{REF\,s0.5}$) was

162   generated by coarsening the resolution to 0.5 m.

163   Then, we simulated point clouds that would have been produced by a LiDAR scanning on

164   vegetation corresponding to reference LAD fields under different configurations (number and position

165   of scans). Following Soma et al. (2018) and Pimont et al. (2019), the effective attenuation coefficient

166   λ_{eff} in a given voxel, which is the rate at which beam density is attenuated by vegetation from a given

167   scan position, relates to LAD_{REF} as follows:

$$\lambda_{eff} = \frac{G}{FH} LAD_{REF} \qquad\qquad (1)$$

168   where G is the leaf projection function, F is the leaf fraction and H is a calibration function

169   which accounts for both voxel size and distance to scanner. To simulate the influence of these factors

170   on LAD estimation, we computed the distribution of effective attenuation coefficient (λ_{eff}) for each

171   scan position, which corresponds to the perception of LAD_{REF} by the instrument. In order to remain

172   representative of typical field conditions, a maximum of 5 scans was performed in a 10 m X 10 m

173   virtual scene. Then for each scan position, the traversal algorithm was applied to the λ_{eff}-3D field to

174   simulate the perceived point clouds, following parameters arising from vegetation and scanner

175   properties (Eq. 1). The details of the point cloud simulations are presented in section 2.3.

176   Finally, LAD estimates were retrieved from these point clouds with different voxel sizes using a

177   traversal algorithm and calibrations provided by field experiments (Soma et al., 2018). The

178   information from multiple scans was combined using the formulation of Pimont et al., (2019) (section

179   2.4). The last section 2.5 describes how we analyzed bias and errors in these estimations. A workflow

180   diagram picturing the methodology used in this work is available in Figure 1.
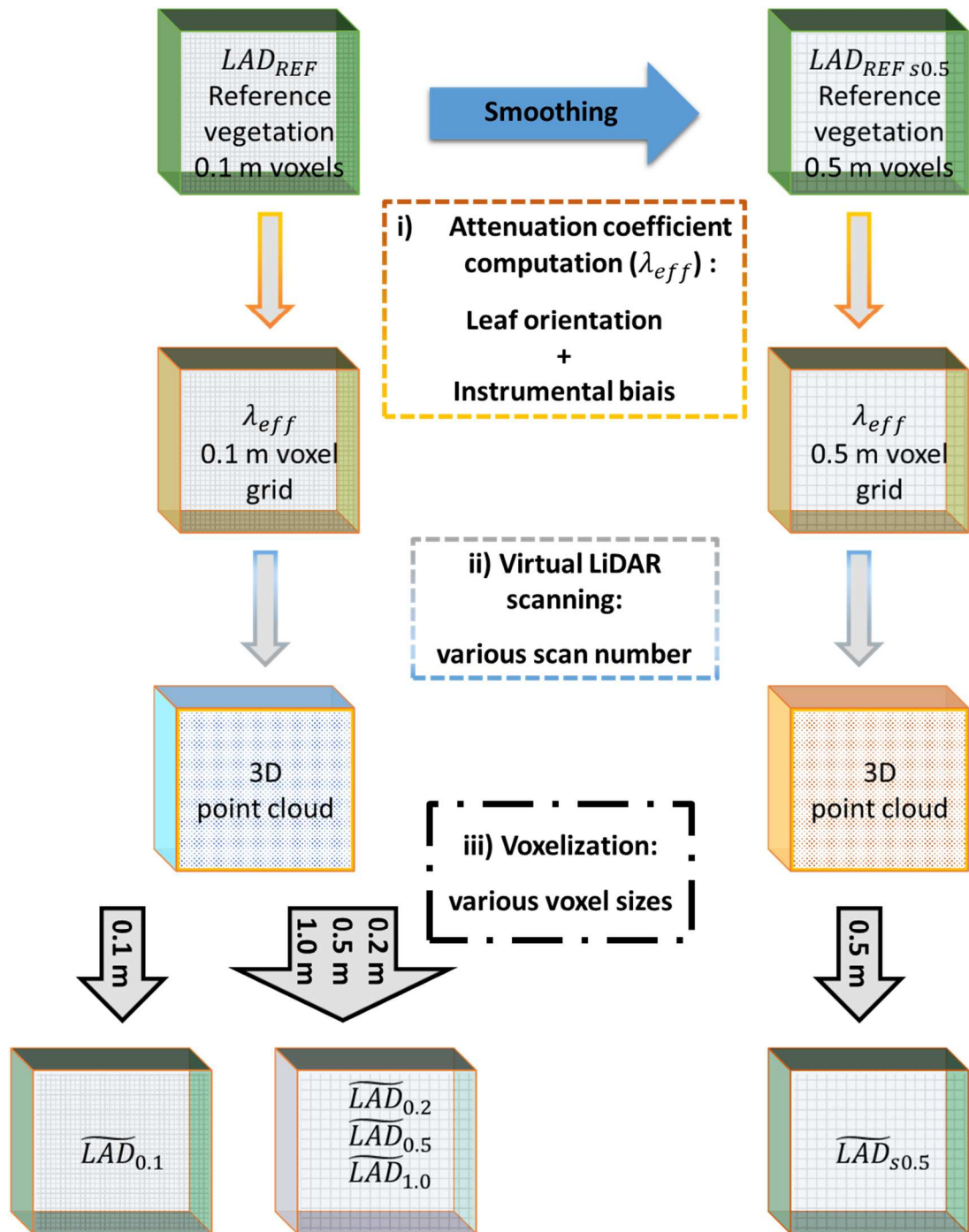
Figure 1. Workflow diagram of simulated LAD scenes and used references. LAD_{REF} is the vegetation reference distribution at 0.1 m heterogeneity scale. $LAD_{REF\,s0.5}$ is the same reference distribution, but at 0.5 m heterogeneity scale. λ_{eff} is the attenuation coefficient. $\widetilde{LAD}$ is the estimated vegetation distribution, with voxel sizes in subscripts.

2.2. Vegetation scene

188   A 3D virtual vegetation scene described from voxelized LAD_{REF} values was generated from a

189 clumped spatial distribution simulated with *RandomFields* R package (Schlather et al., 2015) in a grid

190 with 0.1 m resolution. The mean clump size, representative of tree crown diameter, was 4 m. This

191 virtual scene was cubic with an extent of 10 m in each grid dimension. The canopy height was thus

192 *h*=10 m. The voxel size was set to 0.1 m.

193   The vegetation scene included a realistic vertical profile, with little vegetation below 3 m, an

194 increase to a maximum of LAD values at 7 m, and a decrease until top canopy (see Appendix A). This

195 scene also included random occurrences of 1 m extent local decreases in LAD, with gaps (LAD equals

196 to zero) in 30% of the voxels. This resulted in a vegetation scene with a 70% cover fraction with

197 spatial aggregates corresponding to plant clumps (Figure 2). Such gap distribution was built to

198 analyze the effect of intermediate scale heterogeneity in tree crowns (see spatial correlation in

199 Appendix B). The LAI of the virtual scene was about 3.8, which corresponds to a mean LAD of 0.38

200 m^{-1} (the scene vertical extent was 10 m). Maximal LAD values reached 3.8 m^{-1}. These vegetation

201 properties match the field measurements of a long-term experimental site characteristic of

202 Mediterranean ecosystems (Simioni et al., 2016). The same scene was formerly used in Soma et al.

203 2020, to evaluate the effect of a kriging method for unsampled voxels (Soma et al. 2020).

204   A leaf projection function was implemented to complete vegetation properties following:

$$G(\theta, z) = \frac{1}{2} + 0.4 \frac{z}{h} \cos(2\theta) \tag{2}$$

205 where θ is the angle between the beams and the vertical and ranges between 0 and π. According to

206 this setting leaves are planophile near the canopy top ($z \approx h$), with G=0.9 for vertical beams ($\theta \approx 0$

207 or $\theta \approx \pi$) and 0.1 for horizontal beams ($\theta \approx \frac{\pi}{2}$), and random near the ground ($z \approx 0$), with G=0.5.

208   At last, leaf fraction was parameterized to account for fine woody material and leaf association

209 along vertical axis following:

$$F(z) = \left(0.1 + 0.8 \frac{z}{h}\right)^2 \tag{3}$$

210 Leaf fraction was hence 0.9 at canopy top ($z \approx h$) and 0.1 near the ground ($z \approx 0$).

211

212
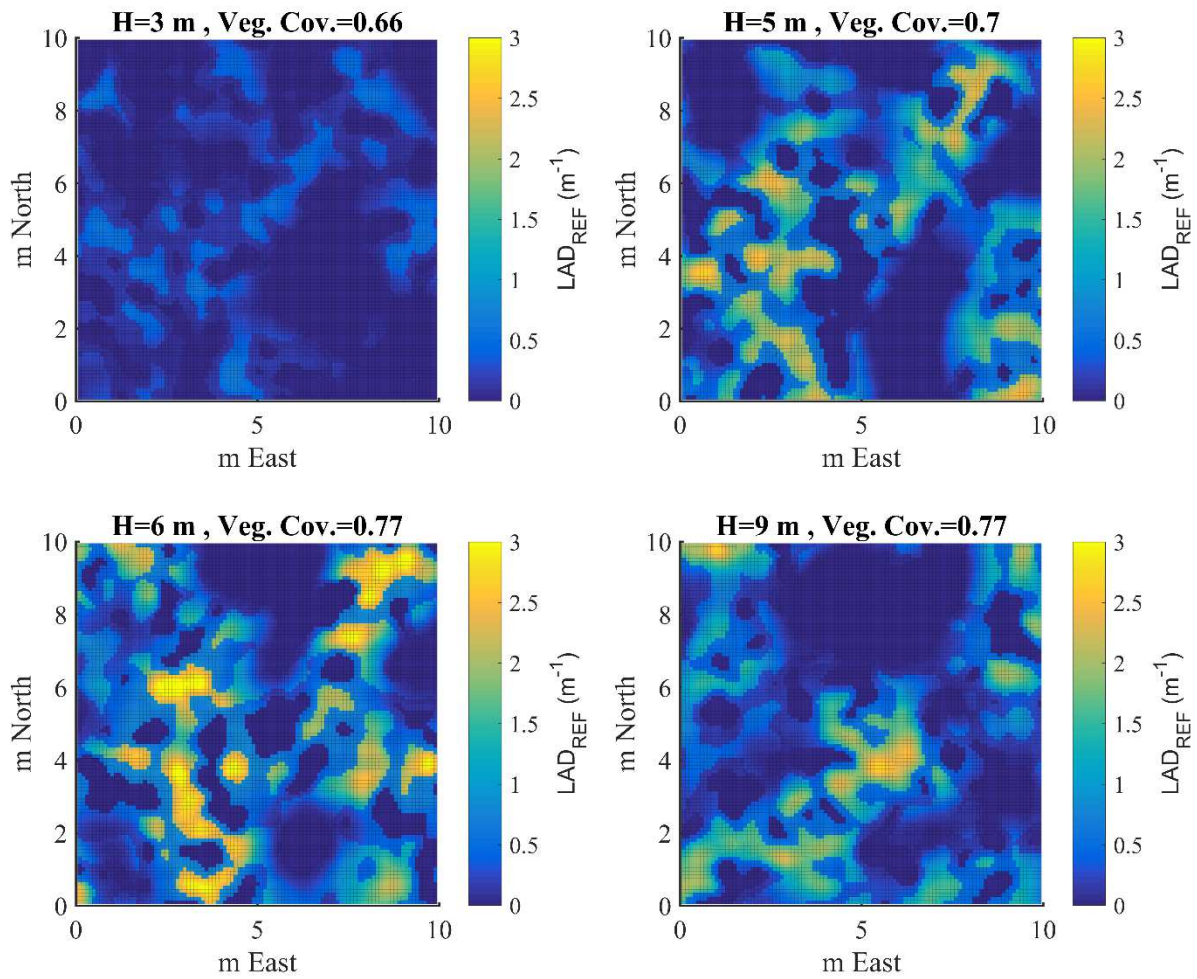
Figure 2. Reference horizontal distributions of LAD_{REF} at 4 different heights. Heights (H) of the mapped layer and associated vegetation cover fractions are indicated in titles. Colors are scaled on LAD_{REF} values from low to high densities (blue to yellow, respectively). A three dimensional view is available in Appendix C.

218

2.3. Simulation of a virtual point cloud corresponding to LAD_{REF} field

Simulation of virtual point clouds were based on turbid media assumption, which states that the probability of a beam to be intercepted increases exponentially with the optical depth (product of attenuation coefficient and distance travelled). The locations in which individual laser beams are intercepted are thus generated from the simulation of free paths (distance travelled before interception)

224 from random numbers following probabilistic laws which account for vegetation density, as done for

225 example in Pimont et al. (2018) within a single voxel. Here the approach is generalized to a

226 heterogeneous scene, corresponding to an idealized forest plot with a spatially-correlated LAD field.

227 The process is iterated in the different voxels travelled along the beam pass, for all beams according to

228 the shooting pattern of the instrument representative of TLS field sampling of a forest plots.

229

230 *2.3.1 Effective attenuation coefficient $\lambda_{eff,j}$ corresponding to a given scan j*

231 The reference vegetation scene is the voxelized *LAD_REF* distribution described above. For

232 simplicity, we assume that the size of vegetation elements (Beer law's approximation) and the volume

233 of voxel occupied by wood elements are negligible. This allows simple framework adequate for

234 testing sampling effect at stand-scale, but both factors can be rigorously accounted for, as shown in

235 Pimont et al. (2019). As detailed above (Eq. 1), the reference attenuation coefficient $\lambda_{eff,j}$ related to

236 *LAD_REF* for a given scan j depends on leaf projection, leaf fraction, vegetation heterogeneity and

237 scanner properties. Yet, the probability of interception of laser beams depends exclusively on $\lambda_{eff,j}$,

238 not directly on *LAD_REF*. To proceed to a realistic point cloud simulation and account for various

239 distances between voxels and scan positions, the $\lambda_{eff,j}$ has to be computed at each voxel for each

240 viewpoint j according to Eq. 1.

241 Let (x_j, y_j, z_j) be the coordinates of the scanner corresponding to scan j and (x, y, z) the

242 coordinates of the center of a voxel in the vegetation scene. Following Eq.1 and according to the

243 vegetation definition above, the effective attenuation coefficient for both leaf and wood for scan j is:

244

245

$$\lambda_{eff,j}(x,y,z) = LAD_{ref}(x,y,z) \frac{G_j(x,y,z)}{F(z)H_j(x,y,z)} \qquad (4)$$

246

247

248   A beam emitted from the scanner that would go in the direction of this point has the following

249   projection function G (since $\cos(2\theta) = \cos(\theta)^2 - \sin(\theta)^2$):

250

$$G_j(x,y,z) = \frac{1}{2} + 0.4\frac{z}{h}\frac{(z - z_j)^2 - (x - x_j)^2 - (y - y_j)^2}{(x - x_j)^2 + (y - y_j)^2 + (z - z_j)^2} \tag{5}$$

251

252   We assumed that the distance effect (caused by an increase in effective footprint of the scanner, as

253   identified in Soma et al. 2018)) have the following effect on the attenuation coefficient:

254

$$H_j(x,y,z) = 1 - 0.05\sqrt{(x - x_j)^2 + (y - y_j)^2 + (z - z_j)^2} \tag{6}$$

255

256   which expresses that vegetation area is overestimated by a factor 2 at a distance of 10 m to the scanner

257   (H_j=0.5). The reference LAD_{REF} field used to compute $\lambda_{eff,j}$ in presented in Figure 2. at 0.10 m

258   discretization level (see section 4.5 for details).

259

260   *2.3.2 Point cloud simulations*

261   From the effective attenuation coefficient distribution (Eq. 15), we can simulate a virtual point

262   cloud based on free path distribution simulations, as explained below. We assumed that function in

263   (Eq. 15) can be discretized in a 3D computational grid ($\lambda_{eff,j}$ assumed to be constant within a

264   computation cell, its value being equals to (Eq. 17) with (x,y,z) from cell center coordinate) with

265   vegetation elements much smaller than grid size (turbid medium assumption).

266   Five scans were simulated. For each scan configuration, scans positions were placed with respect to

267   optimal scene sampling coverage, similarly as field experiment would be, with the potential exception

268   of absence of dense vegetation under 3m. All scans were placed at 1 m from the ground. 4 scans were

269   placed close to each corner of the plot and one scan at the center:

270          $(x_1,y_1,z_1) = (7.5,7.5,1)$; $(x_2,y_2,z_2) = (7.5,2.5,1)$; $(x_3,y_3,z_3) = (2.5,2.5,1)$;

271       $(x_4,y_4,z_4) = (2.5,7.5,1)$; $(x_5,y_5,z_5) = (5,5,1)$.

272   We also parameterized their shooting pattern as follows. Their angular resolution was 0.05° over the

273   horizontal (ranging from 0 to 180°) and the vertical (ranging from 0 to 360°), so that each scan

274   contains 66 million beams, which is typical of the resolution used in the field (e.g. Pimont et al. 2015).

275   For each beam, we simulated its eventual hit position as follows: First, optical path (i.e. initial

276   potential to pass through vegetation) of each beam was randomly simulated according to Beer-

277   Lambert law (assuming infinitely small elements):

278

$$l = -\log(p) \tag{7}$$

279   with p a random number between]0;1[(i.e. initial random chance to be intercepted by vegetation).

280

281   We then computed the trajectory of this beam within the computation grid, from its initial position at

282   scanner location, by computing the "amount" of optical path required to cross the next voxel. This

283   amount was calculated by multiplying the effective attenuation coefficient of this voxel by the length

284   of the segment corresponding to the intersection of the beam and the voxel. When the residual optical

285   path of the beam was shorter than this amount, a hit occurred within this voxel at a location

286   corresponding to this residual optical path. On the contrary, when the remaining optical path was

287   greater than this amount, it means that the beam travelled farther than the voxel. The process was

288   recursively applied to the next voxel, the "new" residual optical path corresponding to the remaining

289   of the previous one. The process ends in case of hit or when a beam reached the bounding box of the

290   computational grid. In this later case, the beam was never intercepted in the computational grid, thus

291   corresponding to a beam with no hit. This process is similar to the one used by (Pimont et al., 2009) to

292   simulate photons trajectories to compute the radiative transfer from a flame through a voxelized

293   heterogeneous vegetation scene with a MonteCarlo approach.

294

295   This process was repeated for each scan position. Hence, five virtual point clouds were

296   simulated in accordance with $\lambda_{eff,j}$, which accounts for both vegetation and instrument properties.

297

13

298   *2.4.   Computation of LAD estimates for simulated point clouds including unsampled voxels*

299   For each viewpoint j, we used a traversal algorithm developed under Matlab software (The

300   MathWorks, Inc., Natick, MA, USA). For each scan, intersections between each beam (i.e. line

301   between hit and scan position) and the voxel grid were computed in order to retrieve the following

302   metrics in each voxel: Ni_j the number of hits in the voxel, $\sum z_j$ the sum of free paths, $\sum_{hit} z_j$ the sum

303   of free paths corresponding to hits only.
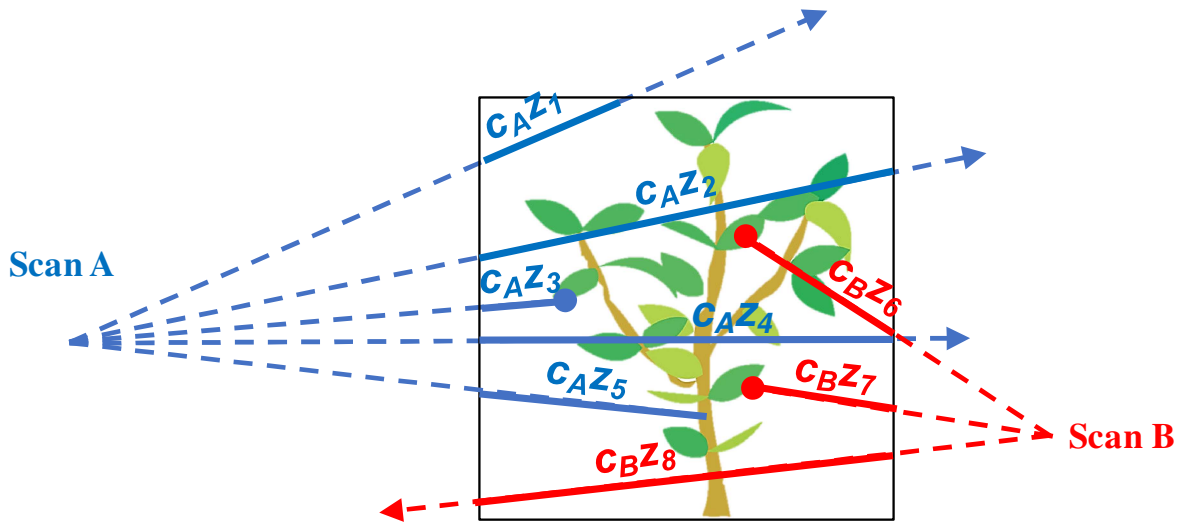
304

305   **Figure 3.** Scheme of the information provided by the traversal algorithm which is used to compute the

306   unbiased estimator of *LAD* from multiview data from Scan A (in blue) and Scan B (in red): leaf hits

307   (blue and red dots) and free paths (distances z travelled by the beams, blue and red lines) in the voxel.

308   The dotted lines represent pulse trajectories. c_A and c_B represent the correcting factors for viewpoints A

309   and B, which depend on distance to scanner and view angle (see Pimont et al., 2019 for details).

310

311   From these quantities, we can define in each voxel the following "multi scan" quantities, using known

312   values of G, H and F:

313   - $Ni = \sum_j Ni_j$ the total number of hits

314   - $\sum \frac{G}{H} z = \sum_j \frac{G_j}{H_j} \sum z_j$ the total free path sum, with multiplicative correction factors.

315   - $\sum_{hits} \frac{G}{H} z = \sum_j \frac{G_j}{H_j} \sum_{hit} z_j$ the total "hit" free path sum, with multiplicative correction factors.

14

316 Following Pimont et al. (2019, Eq. 13), we used the following unbiased point estimator of LAD,

317 provided that N was larger than 2:

$$\widehat{LAD} = \frac{F}{\sum \frac{G}{H} z}\left(\text{Ni} - \frac{\sum_{hits}\frac{G}{H}z}{\sum \frac{G}{H}z}\right) \tag{8}$$

318 In this formulation, $\frac{\sum_{hit}\frac{G}{H}z}{\sum\frac{G}{H}z}$ is a biais correction term ranging between 0 and 1, so that the estimator is

319 simply $\frac{FNi}{\sum\frac{G}{H}z}$ when Ni is large, which corresponds to the Maximum Likelihood Estimator (Pimont et al.

320 2018). This formulation also accounts for leaf orientation, wood and instrument specifications (Pimont

321 et al. 2019). This estimator generalizes the Modified Contact Frequency proposed by Béland et al.

322 (2011) with the bias correction term to account for low sampling, leading to an unbiased point

323 estimator provided that more than 2 beams are available (Pimont et al. 2018). The voxels with N

324 smaller or equal to 1 were considered as unsampled, because no unbiased estimator has been

325 suggested for N=1 (Pimont et al. 2019). Indeed, Eq. 8 leads to estimates of 0 when N=1, even when

326 Ni=1, which is obviously negatively biased. As a result, voxels with N lower than 2 were considered

327 as unsampled. For unsampled voxels, we used the "mean layer value" to estimate LAD, which was

328 computed from the mean of $\widehat{LAD}$ (computed for N larger or equal than 2). This method for dealing

329 with unsampled voxels is the most widely used (Béland et al., 2014b; Schneider et al., 2019).

330 We also computed the radius of the 68% confidence interval for $\widehat{LAD}$, which can be estimated by

331 (Pimont et al. 2019):

$$\Delta\widehat{LAD} = \frac{F\left(\text{Ni} - \frac{\sum_{hits}\frac{G}{H}z}{\sum\frac{G}{H}z}\right) + \frac{1}{2}}{\sqrt{F\text{Ni} + \frac{1}{2}\sum\frac{G}{H}z\left(1 + \frac{1}{N}\right)}} \tag{9}$$

332 with $N = \sum_j N_j$ the total number of beams entering a voxel.

333

334 *2.5. Analysis of estimations*

335

Table 1. Description of the different simulations. They differ both in the reference vegetation field used to generate the virtual point cloud (ray-tracing algorithm) and in the voxel size used for the estimation process.

Reference vegetation used to generate the virtual point cloud (scale in m)	Voxel size used for estimation	Estimations
LAD_{REF} (0.1 m)	0.1 m	$\widehat{LAD}_{0.1}$
LAD_{REF} (0.1 m)	0.2 m	$\widehat{LAD}_{0.2}$
LAD_{REF} (0.1 m)	0.5 m	$\widehat{LAD}_{0.5}$
LAD_{REF} (0.1 m)	1.0 m	$\widehat{LAD}_{1.0}$
$LAD_{REF\ s0.5}$ (0.5 m)	0.5 m	$\widehat{LAD}_{s0.5}$

LAD_{REF} corresponds to the reference vegetation field defined at 0.1 m resolution. $LAD_{REF\ s0.5}$ corresponds to a manipulation of LAD_{REF}, which was smoothed at 0.5 m. As the scale of heterogeneity in these different reference fields differ, the subsequent virtual point clouds are also different.

2.5.1 Exploring bias arising from vegetation heterogeneity

It has been suggested that ignoring clumping effect within voxel could lead to strong LAD underestimation (Béland et al., 2014a; Soma et al., 2018). This bias depends on voxel size, large voxels being more prone to aggregate gaps and clumps within voxel volume. In the present study, we analysed the effect of voxel size by comparing estimates obtained with voxel sizes ranging from 0.10 m to 1 m to reference values (section 5.4). This analysis relied on mean estimated vertical profiles (i.e. estimates were averaged by height layers). For each voxel size, the correction factor required to match reference value was derived at all heights. One of the drawback of a basic sensitivity analysis to voxel size is that it does not disentangle the effects of vegetation heterogeneity (i.e. Jensen's inequality) and sampling limitations (i.e. more or less beams exploring voxels). In order to minimize the role of sampling limitations in the voxel size analysis, we only used estimations derived from the maximum sampling level, i.e. 5 scans design. To unravel the effect of subgrid vegetation heterogeneity, LAD estimations with 0.5 m voxels were performed both on original LAD_{REF} and on

356 $LAD_{REF\ s0.5}$. By definition, $LAD_{REF\ s0.5}$ field was manipulated (smoothing) so that it does not include

357 any vegetation heterogeneity below 0.5 m. This result is presented in section 3.3. Then the magnitude

358 of vegetation heterogeneity effect is characterized in section 3.4 by comparing LAD estimations

359 retrieved with tested voxel sizes on vegetation resolved at 0.1 m scale (i.e. $\widehat{LAD}_{0.1}$ to $\widehat{LAD}_{1.0}$

360 compared to LAD_{REF}).

361   *2.5.2 Consequences of sampling limitations*

362   To provide insights regarding limitation associated with sampling in this context, we evaluated the

363 sensitivity of estimates to the number of scans (different scan designs, from a single viewpoint to 5

364 scans) in sections 3.4. and 3.5. The single scan configuration used the scanner in central position, the

365 two scans configuration used opposite diagonal design (top left to bottom right), the three scans

366 configuration used full diagonal design and the four scans configuration used corners positions and

367 five scan design used all positions.

368   Additionally, in order to perform a cross analysis between voxel size and number of scans, each

369 scan configuration was used at both 0.10 m and 0.5 m voxel sizes. To disentangle the effect of

370 sampling from the effect of vegetation heterogeneity (see 2.5.1), we used $LAD_{REF\ s0.5}$ field for LAD

371 estimations with 0.5 m voxel (i.e. $\widehat{LAD}_{s0.5}$), similarly to section 2.5.1. Therefore, differences between

372 estimates in section 3.5 cannot be attributed to a potential effect of vegetation heterogeneity effect, but

373 only to sampling. Analyses of estimated vertical profiles were performed similarly to analysis of voxel

374 size bias. For the computation of the vertical profile, we remind that the unsampled voxels were

375 estimated by the "mean layer value". One should notice that in practice, LAD profiles computed from

376 all voxels (including unsampled voxels estimated with the "mean layer method") provide identical

377 profiles to those computed with means based on sampled voxels only.

378

379 All configurations were tested against references. Evaluations were performed through the comparison

380 of mean layer $\widehat{LAD}$ profile and mean absolute error (MAE). For a given set of voxels or layer *i*, MAE

381 was computed according to:

382          $MAE_i = \dfrac{\overline{|LAD_{REF,i} - \widehat{LAD_i}|}}{\overline{LAD_{REF,i}}}$ (10)
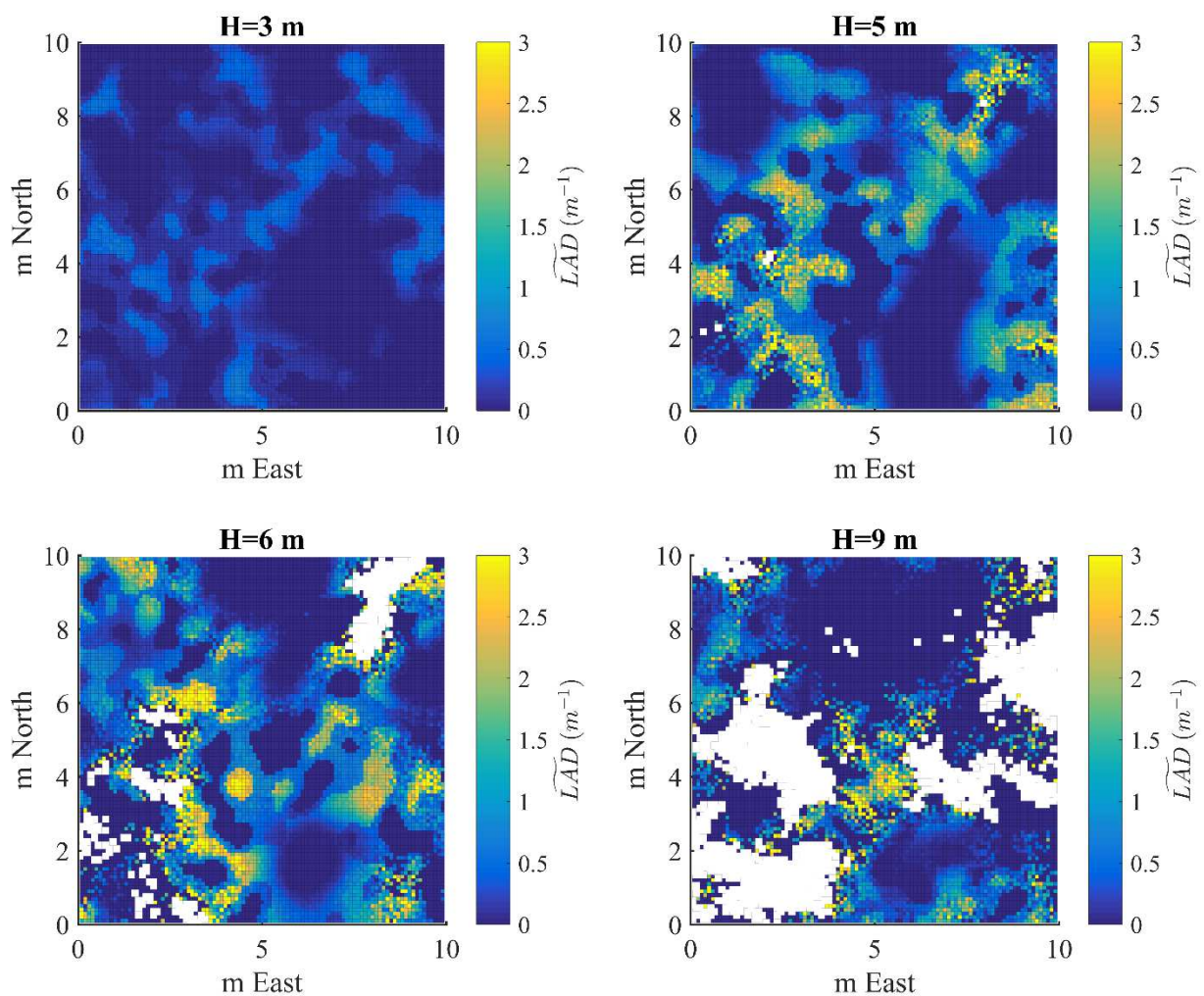
383

384   Additionally, we analyzed the distribution of 68%-confidence interval radius (Eq. 9) to evaluate

385   efficiency of local estimates for various scans and voxel sizes configurations.

386

387   **3.   Results**

388   *3.1.   Overview of LAD patterns estimation*

389

391   **Figure 4.** Estimated horizontal distribution of $\widehat{LAD}_{0.1}$ at four heights. Heights (H) of the mapped layer

392   and associated vegetation covers are indicated in titles. Colors are scaled on $\widehat{LAD}$ values from low to

393   high densities (blue to yellow, respectively). These distributions can directly be compared to subplots

18

394   in Fig. 1 (LAD_{REF}). Here, the traversal algorithm was applied to the five scans at a 0.10 m voxel size.

395   Blank pixels are unexplored voxels, which reveal occluded locations in the upper part of the canopy.

396

397   Figure 4 shows horizontal distributions of LAD estimations at four heights above ground

398   level, providing insights on the 3D distribution of $\widehat{LAD}_{0.1}$ at plot scale. Comparison with the same

399   plots shown for LAD_{REF} in Figure 2 allowed to identify main discrepancies with the reference field. At

400   low height (H=3 m), estimates were very close to the reference for all voxels. From 5 m height and

401   above, the general structure and variability in the LAD distribution was captured, but a few

402   discrepancies can be identified. In particular, horizontal variations in $\widehat{LAD}_{0.1}$ were less smooth than the

403   reference, with inaccuracy resulting from poor sampling. Typically, local differences were identified,

404   mostly visible in dense clumps and a few voxels that were not sampled (in white). At 6 m height, some

405   large blocks of unexplored voxels occurred, most of them being located in dense locations (LAD

406   higher than 2 m^{-1}). In upper canopy (H=9 m), large errors occurred (higher than 100%) and unexplored

407   voxels were very frequent (~30% of voxels). These unexplored locations were typically structured in

408   large blocks (until 4-m width), covering both dense and light vegetation density.

409   The following sections provide quantitative analyses of estimations under various configurations.

410

3.2. Influence of unsampled voxels (mean layer estimates)

412
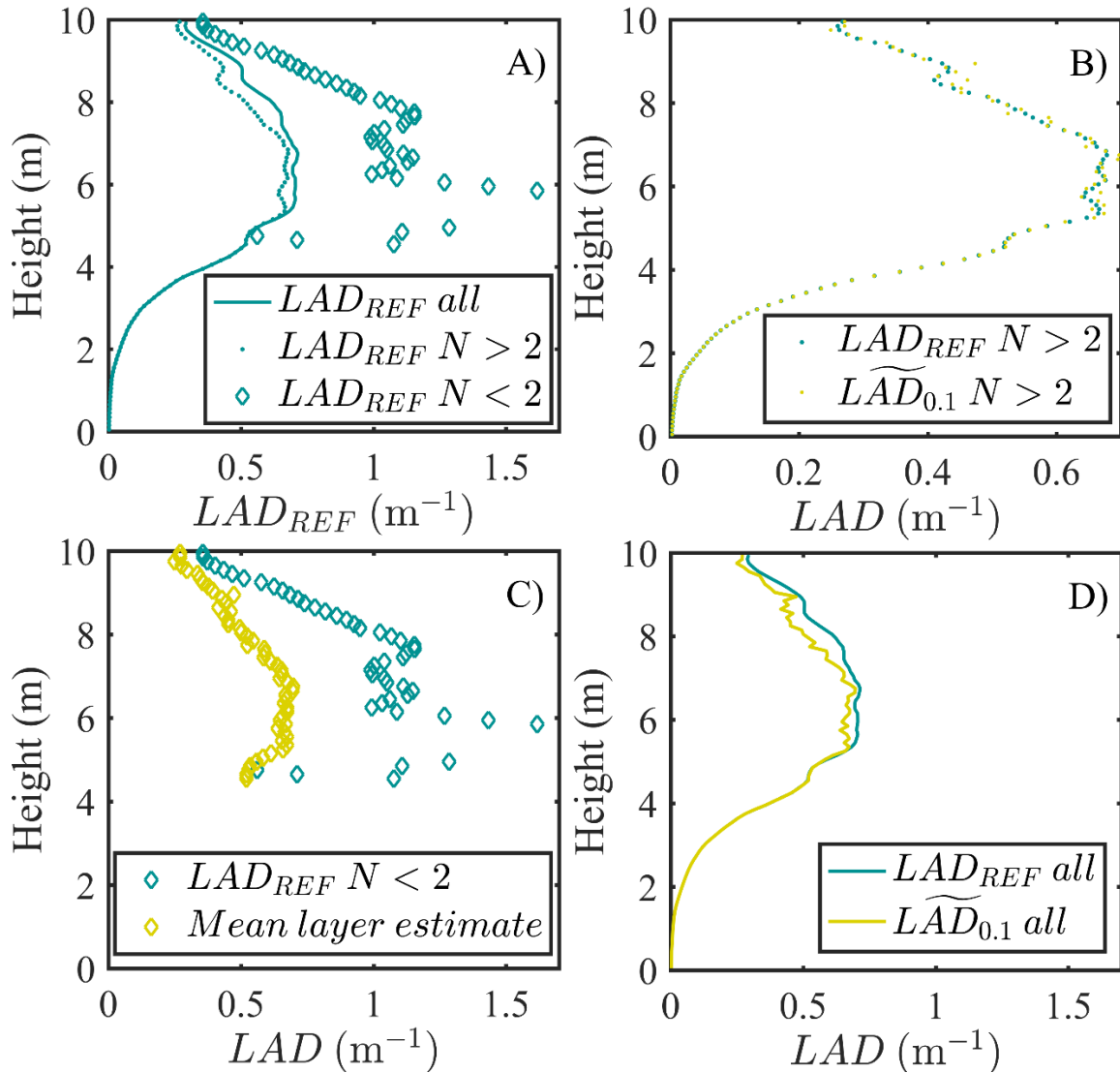
Figure 5. Comparison of LAD profiles at 0.1 m voxel size with 5 scans. A) Comparison of LAD_{REF} profiles for all voxels (blue curve), sampled voxels (N>2, blue dots) and unsampled voxels (N<2 (blue diamonds). B) Comparison of LAD_{REF} and $\widetilde{LAD}_{0.1}$ from sampled voxels (N>2, blue and yellow dots, respectively). C) Comparison of LAD_{REF} and $\widetilde{LAD}_{0.1}$ from unsampled (N<2, blue and yellow dots, respectively). D) Comparison of LAD_{REF} and $\widetilde{LAD}_{0.1}$ profiles with all voxels (blue and red yellow, respectively).

In this section, we consider LAD estimations of LAD_{REF} at 0.1 m voxel size. Therefore, we must not expect any effect of subgrid vegetation heterogeneity on estimations, as this is exactly the resolution

of the reference field. Figure 5 compares profiles obtained for references and estimated voxels, which

were respectively explored by less or more than 5 beams. The analysis of reference profiles (**Fig5A**)

allowed to pinpoint sampling quality differences depending on reference LAD values. As expected,

the unsampled voxels at a given height exhibited systematically the highest reference LAD values,

well above the mean LAD_{REF} (**Fig5A**), and were systematically underestimated, because the "mean

layer" value (that was attributed to unsampled voxels) was strictly lower than actual references in

unsampled voxels (**Fig5C**). For explored voxels, the agreement between the reference and the

estimation was very good (**Fig5B**), which confirms the unbiasness of point estimates used in the

present study (initially proposed by Pimont et al. 2018). This demonstrates that the overall

underestimation (**Fig5D**) was caused by unsampled voxels (even if the "mean layer" value was

assessed to these voxels). This confirms the hypothesis presented in introduction, where we suggested

that the heterogeneity of sampling was likely to induce biases in mean estimates. Moreover, these

differences in LAD_{REF} between sampled and unsampled voxels decreased in the upper part of the

canopy (**Fig5A**). Hence voxels had similar averages near canopy top. This suggests that sampling

restriction was a random process where occlusion was very severe (in the upper part), contrary to

where occlusion began (mid canopy), where occlusion concerned more frequently the denser voxels.

3.3. Influence of subgrid vegetation heterogeneity
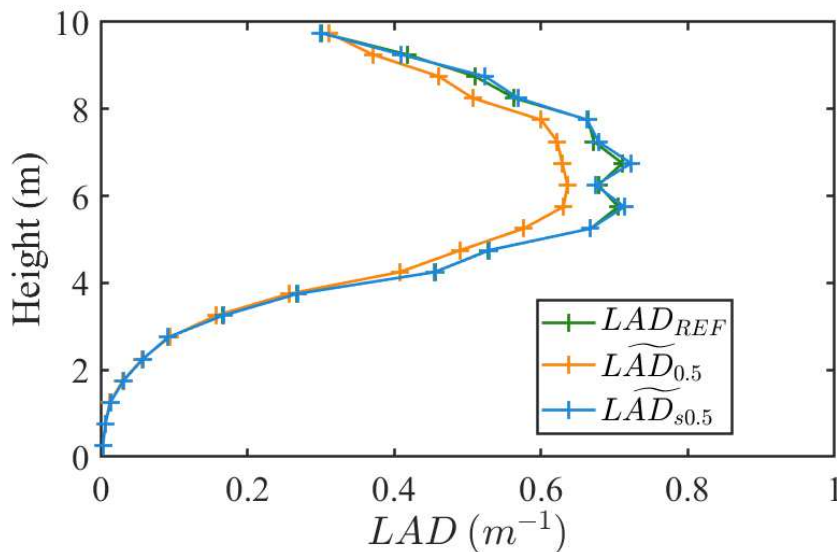
Figure 6. Comparison of five scans design profiles of $\widehat{LAD}_{0.5}$ and $\widehat{LAD}_{s0.5}$ (generated from the smoothed reference $LAD_{REF\,s0.5}$) with the reference LAD_{REF}. Profiles were averaged in 0.5-m layer to ease comparisons, so that a single reference could be used for both estimates (labelled LAD_{REF} for simplicity), as $LAD_{REF\,s0.5}$ and LAD_{REF} were identical at the 0.5 m resolution by definition.

At coarser voxel sizes, convexity effects associated with subgrid vegetation heterogeneity are expected to affect LAD estimations, also leading to underestimations when, for example, comparing $\widehat{LAD}_{0.5}$ to references (Figure 6). However, a part of this negative bias could have been caused by the presence of unsampled voxels. In order to formerly attribute this negative bias to subgrid vegetation heterogeneity, we used the estimates ($\widehat{LAD}_{s0.5}$) derived from smoothed reference fields $LAD_{REF\,s0.5}$ (Figure 6), corresponding to a scenario in which no subgrid vegetation heterogeneity can occur. In this case, estimates ($\widehat{LAD}_{s0.5}$) were very close to reference profile, demonstrating that the role of the sampling bias was negligible in this scenario. The negative bias observed with $\widehat{LAD}_{0.5}$ was hence attributed to subgrid vegetation heterogeneity.

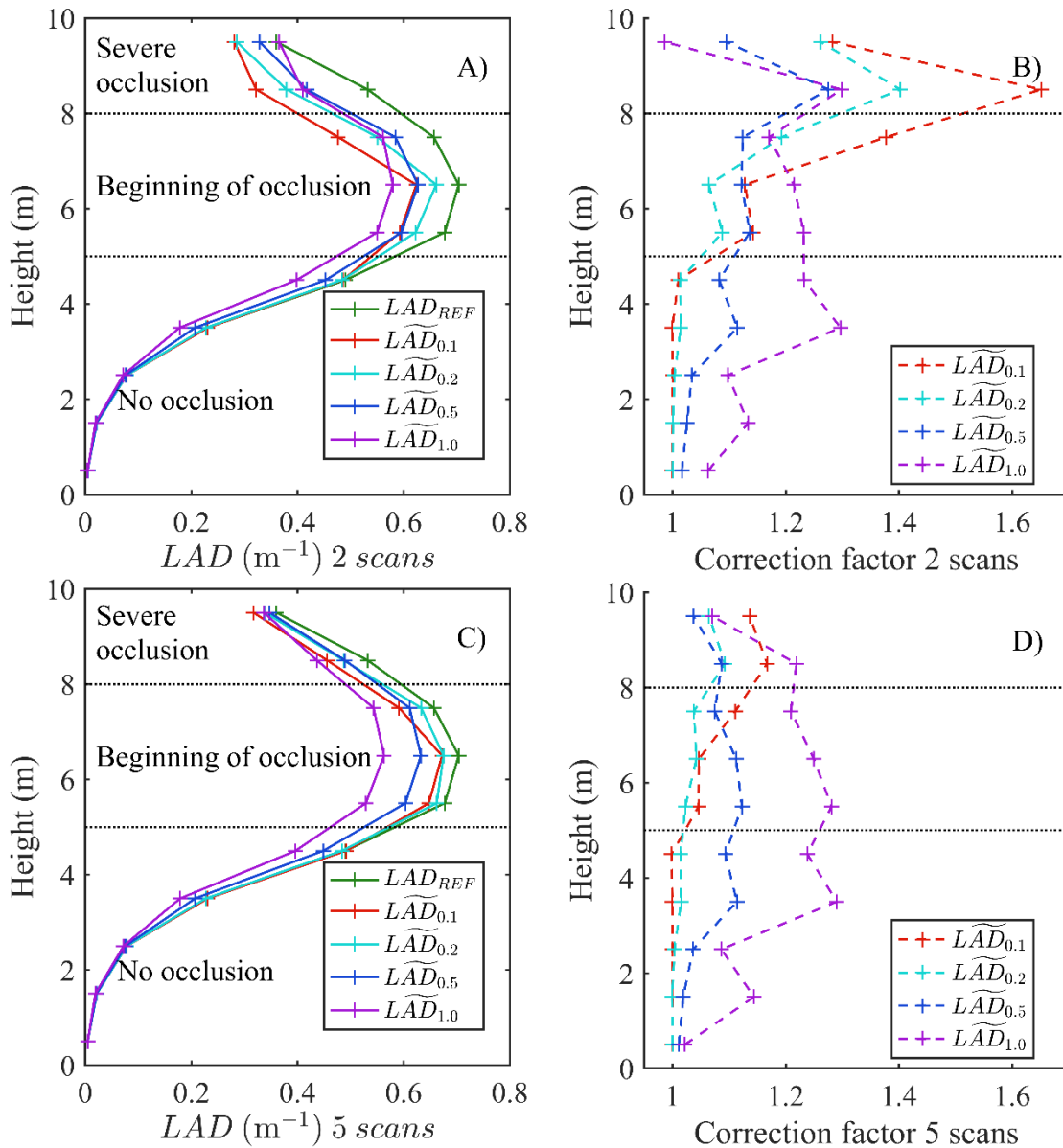*3.4. Overall sensitivity of estimation to voxel sizes*

Because subgrid vegetation heterogeneity and sampling depends on voxel size, the amplitude of negative biases is expected to vary with voxel size, which is investigated in next section.

22

Figure 7. A) Vertical profiles retrieved with $\widetilde{LAD}$ estimates with various voxel sizes for the two scans design. B) Vertical profiles of the multiplicative correction coefficient required to retrieve reference value ($\frac{LAD_{REF}}{\widetilde{LAD}}$) using the two scan design. C) and D) Same as A and B, but for the five scans design. In these plots, LAD were averaged in 1-m layer when voxel size was smaller than 1 m to ease comparison between estimates across voxel sizes. Dotted lines roughly pinpoint height boundaries between layers with no occlusion, layers where occlusion starts to occur (typically within vegetation clumps) and layers with widespread occlusion patterns (both within and outside vegetation clumps).

470   In Figure **7A**, we show the overall sensitivity of estimates of $\widetilde{LAD}$ profiles to voxel size,

471   including both sampling and subgrid vegetation heterogeneity biases, for two scans and five scans

472   designs. All voxel sizes adequately captured the shape of the reference profile. However, various

473   amplitudes of underestimations were observed depending on voxel sizes, scan design and height in the

474   canopy. The significance of these effects was confirmed by a statistical analysis (Appendix D). In

475   well explored layers, i.e. below 5 m, coarser voxel sizes led to strong underestimations, requiring

476   highest correction factors for both scan designs. However, as occlusion occurred and increased in

477   highest layers, the two smallest voxel sizes yielded strongest and variable underestimations, of greater

478   magnitude than with the 0.5 m and 1 m voxel sizes (7B). On the contrary, even in mid and top layers,

479   the biases observed with 0.5 m and 1 m voxel sizes were similar to those below 5 m, resulting in a

480   relatively homogenous bias in the whole canopy.

481   According to the results of previous sections 3.2 and 3.3, underestimations resulted from two

482   different mechanisms, namely, sampling bias for small voxels (e.g. 0.1 m, **Fig 5**) and convexity bias

483   associated with subgrid vegetation heterogeneity for coarse voxels (e.g. 0.5 m, **Fig 7**). Our analysis

484   and vegetation manipulation allowed to disentangle and quantify these biases. We found that their

485   magnitude and their spatial distribution was variable, but that bias arising from sampling limitations

486   was very unstable and of stronger magnitude.

487

488   *3.5. Sensitivity of estimates to variations in sampling design (without subgrid heterogeneity*

489   *effect)*

490

491
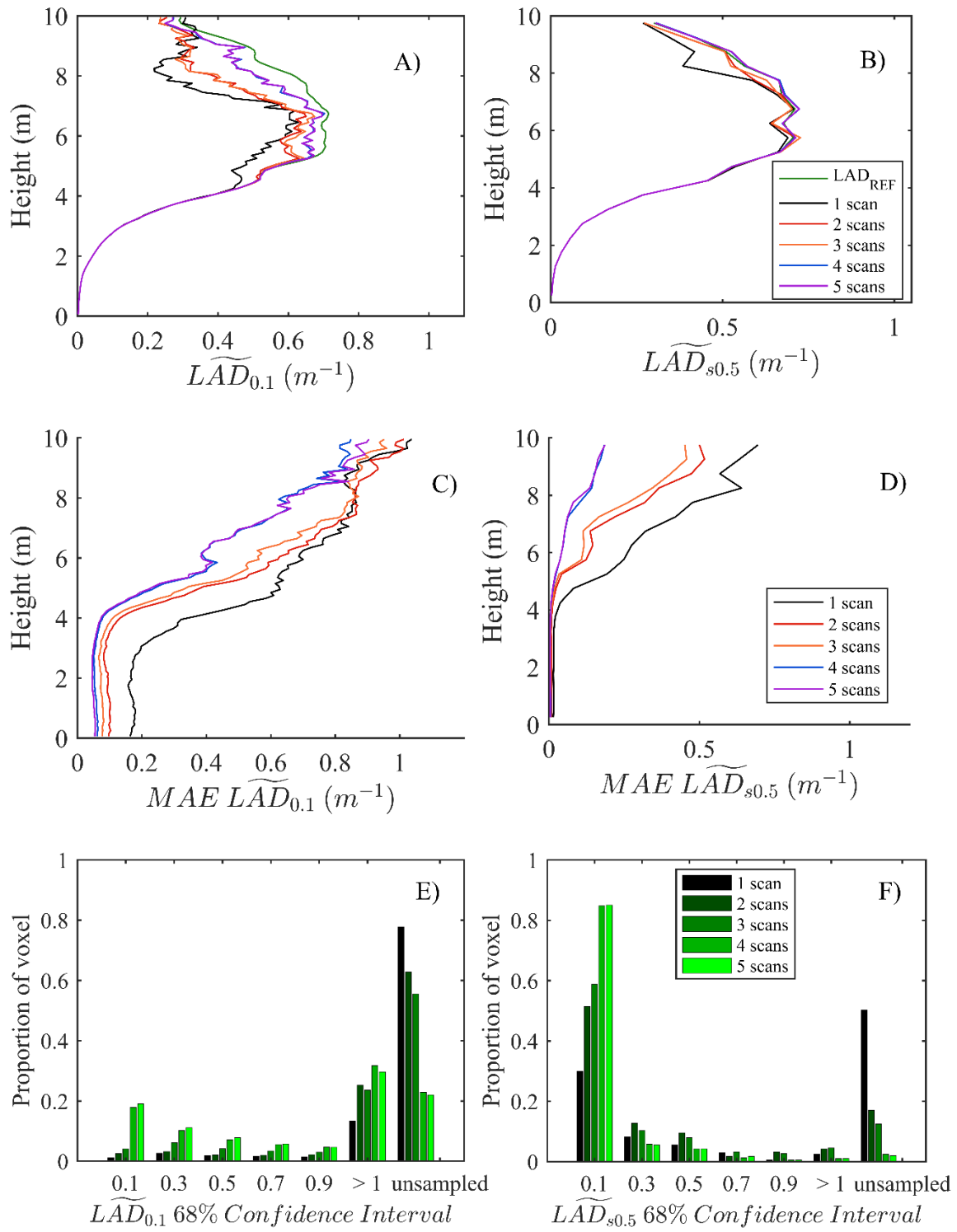
Figure 8. A. Vertical profiles of $\widetilde{\mathrm{LAD}}_{0.1}$ for 1 to 5 scan design. B. Vertical profiles of $\widetilde{\mathrm{LAD}}_{s0.5}$ for 1

to 5 scan designs. Profiles of Mean Absolute Error (MAE, in fraction) are presented accordingly for

each voxel size for $\widetilde{\mathrm{LAD}}_{0.1}$ and $\widetilde{\mathrm{LAD}}_{s0.5}$ in subplots C) and D), respectively. MAE were normalized

by the mean reference values within each horizontal layer. Distributions of 68% confidence intervals

496   with 1 to 5 scan designs (colored bars from black to green, respectively) for $\widehat{LAD}_{0.1}$ and $\widehat{LAD}_{s0.5}$ in

497   subplots C) and D), respectively. Bins have a 0.2 m^{-1} extent centered on x-axis labels.

498

499   Figure 8. presents $\widehat{LAD}$ profiles and corresponding Mean Absolute Error (MAE), for various

500   number of scans (1 to 5 scans design) and two voxel sizes (0.1 m and 0.5 m). Normalized MAE

501   inform on the accuracy of the estimation at voxel scale. For the coarsest resolution, we use the

502   smoothed reference field to eliminate the subgrid vegetation heterogeneity effect.

503   The shape of the reference profile was roughly captured for all scan designs and voxel sizes (**Fig.**

504   **8AB**). Below 8 m, estimations were closer to reference (**Fig. 8AB**) and errors decreased as the voxel

505   size and/or the number of scans increased (**Fig. 8CD**). The negative bias was less pronounced in the

506   upper part of the canopy (above 8 m), as already noticed with large voxels (**Fig 7**), with more

507   randomly distributed occlusion voxels (with regards to voxel density). For example, the bias was the

508   same for 5 and 1 scans for the 0.1m voxel size in the upper part of the canopy (**Fig 8A**). Both 4 and 5

509   scans design yielded relatively close estimates to the reference, but their MAE were very poor in upper

510   canopy layers (~100% error), remaining similar to the single scan design MAE (**Fig 8C**). At 0.5 m

511   voxel size (**Fig 8B**), with the 4 and 5 scan design, the estimated profile (blue and violet lines) closely

512   matched the reference. In this context, coarser voxels exhibit an increased sampling rate with respect

513   to fine voxels (as for multiplying scan positions), leading to significantly better estimated profiles and

514   smaller MAE values (thanks to the suppression of the subgrid vegetation heterogeneity effect).

515   However, the single scan design, and in a lesser extent 2 and 3 scans designs, remained affected by

516   systemic negative bias and large occlusion (drop down of estimations) above 8 m, even with 0.5 m

517   voxels (**Fig 8B**). Conversely to 1-2-3 viewpoints, MAE were much lower than with 0.1 m voxel size

518   and were limited to 0.7 at top height, which showed that the estimated local voxel value was more

519   reliable. Remarkably, the 4-5 scans design had MAE limited to 0.2 at top height, which is consistent

520   with a 20% error on a given voxel in average.

521   Figure **8EF** shows the impact of number of scan and voxel size on the distributions of 68%

522   confidence intervals (CI) in sampled voxels, and on the occurrence of unsampled voxels. Increasing

523   the voxel size and number of scans decreased occurrences of unexplored voxels, as suggested above.

524 In particular, 80% of voxels were unexplored for a single scan at 0.10 m voxel size (i.e. most critical

525 case), implying that estimations relied on only 20% of the vegetation scene. More generally, more

526 than 50% of the voxels are unexplored when three scans or less are used, which highlights that such a

527 0.1 m voxel size is not really practical given TLS resolution and number of scans.

528   For explored voxels, increase in number of scans and voxel sizes tends to decrease CI width,

529 leading to higher frequencies of small errors. In particular, whatever the scan design, increasing the

530 voxel size shifted the occurrence of largest CI (>1) and unexplored voxels (i.e. infinite error) towards

531 the lowest CI values. Typically, the single scan design was almost unable to produce estimations with

532 CI lower than 1 m^{-1} at 0.10 m voxel size, whereas 30% of estimations reached the smallest confidence

533 level with 0.5 m voxel size. Similarly, with the 4-5 scan designs, 20% of the estimates had the smallest

534 confidence level at 0.10 m voxel size, while 85% of voxels are estimated with CI lower than 0.2 m^{-1} at

535 0.5 m voxel size. As a result, at least 50% of the voxels were unexplored with the 0.1 m voxel size,

536 even for 5 scan designs. These points highlight the fact that the sampling used in the present numerical

537 experiment, which was representative of field conditions (a few scans per forestry plot, with 0.036°

538 resolution) was too limited to provide reliable results at the 0.1 m voxel size, contrary to coarser

539 voxels, which on the other hand, raise the problem of subgrid vegetation heterogeneity (**Fig 6**, **Fig 7**).

540

541 **4. Discussion**

542 The simulation framework used in this study allowed to evaluate the process of estimations of LAD

543 with TLS thanks to exact references. In particular, we analysed the sensitivity to vegetation and

544 sampling heterogeneities. We disentangled combined effects associated with variations in voxel sizes

545 and scan designs with respect to true numerical references, and biases were formerly attributed to two

546 main mechanisms, thanks to our numerical design and the used of unbiased point estimators. Our

547 study confirmed the effect associated with subgrid vegetation heterogeneity, which leads to

548 underestimation when voxels are too coarse to explicitly account for it. This effect is discussed in

549 section 4.1. Our study also demonstrates that an overall negative bias can arise when relying on mean

550 layer estimates for correcting for the presence of unsampled voxels. The bias was not homogeneously

551   distributed within the vegetation scene and typically occurs when occlusion begins to be significant (at

552   mid-canopy height in the present example), as it more frequently affects clumps of dense voxels, but

553   can diminish in highest vegetation layer, despite strong occlusion. This effect is discussed in section

554   4.2. Beyond overall biases in vertical profiles, we also studied the sensitivity of voxel-scale

555   predictions to voxel size and scan design, as the objective of voxelized TLS method is to measure the

556   tri-dimensional distribution of the LAD. The distribution of confidence intervals showed that the voxel

557   sizes required for a reasonable accuracy (here typically 0.5m), could be larger than the voxel size

558   required to mitigate subgrid vegetation heterogeneity. The discussion ends with recommendations and

559   future work.

560

561   *4.1. Subgrid vegetation heterogeneity should be accounted for to provide reliable*

562   *estimations*

563

564   In the present study, underestimations occurred when voxel size increased (i.e. 0.5 m, **Fig. 6**),

565   and the negative bias of the estimated LAD profile (i.e. for a horizontal layer of voxels) could reach

566   30% for 1 m voxel size (**Fig. 7**). We found that such underestimation did not occur when point clouds

567   were generated with vegetation that was smoothed at voxel size ($\widehat{LAD}_{s0.5}$, **Fig. 6**), which

568   demonstrated that this effect was caused by subgrid vegetation heterogeneity. This confirms prior

569   observations on natural branches of three different species scanned with two different instruments

570   (Soma et al., 2018), but also on trees (Béland et al., 2014a), which already attributed underestimations

571   to vegetation heterogeneity. One can notice that the effect of voxel size observed in Soma et al. (2018)

572   was more important, requiring a 1.7 correction factor with 0.7 m voxels compared to 1.3 for 0.5 m

573   voxels in the present simulations. Such differences could arise from more heterogeneous vegetation

574   structure in natural vegetation than in our example reference field, in which heterogeneity was

575   resolved at 0.1 m scale. However, these findings demonstrate the efficiency of numerical experiments

576   for testing hypothesis and evidence the associated mechanism (here heterogeneity effect on LAD

577 estimation), since it was possible to numerically manipulate vegetation (here smoothing), for a formal

578 attribution of bias source.

579 Similarly to approaches developed for passive optical measurements (e.g. hemispherical

580 photography), identifying canopy gaps and angular segmentation the scene is efficient to partially

581 correct for clumping (Yan et al., 2019). Yet, the subgrid vegetation heterogeneity in each segment of

582 2D images remains along the optical depth, i.e. in the third dimension. Our results illustrate the

583 potential of an appropriate segmentation level to limit the clumping effect, making TLS voxel-based

584 approaches more efficient compared to 2D gap fraction methods for the separation of gaps and crowns

585 and particularly fitted for application of LAI retrieval approaches, including path length distribution

586 models whether at crown (Hu et al., 2018) or voxel scales (Pimont et al., 2019; Soma et al., 2018).

587

588 *4.2. Sampling limitations generate heterogeneous and variable underestimations*

589

590 When occlusion was limited (typically 5 scans and 0.5 m voxel size), the clumping effect was

591 the main source of underestimation in LAD. However, when sampling limitation became significant,

592 typically above 5 m and with 0.1 m voxels ($\widehat{LAD}_{0.1}$, **Fig 7AB** – red curve), underestimations of

593 heterogeneous magnitudes occurred without any subgrid heterogeneity, demonstrating the presence of

594 a second mechanism of underestimation. This negative bias arose from the spatial correlations

595 between sampling limitations and LAD densities, as clumps of dense volumes were more frequently

596 occluded. Indeed, scan positions located in the open ease the sampling of empty or light voxels and

597 might amplify the oversampling of light voxels described above, while dense voxel are rarely explored

598 and less accounted for in mean layer LAD calculation. This spatial structure of occlusion can result in

599 up to 25% underestimations (**Fig. 8A**) of the average LAD profile despite 5 scans are performed. In

600 these non-sampled volumes, we assigned the mean layer estimated values, which results from sampled

601 voxels in dense layers, i.e. mostly empty and low density voxels, generally equal to 0.4 m^{-1} in average,

602 i.e. much less than dense voxel LAD values. As less and less beams coming from below canopy

603 remained available in the canopy middle, clumps of dense occluded voxels are more frequent, and

604   such underestimation mean bias was worse until 8 m height. Above 9 m, this bias was dampened (**Fig.**

605   **8AB**), because the correlation between dense voxels and occluded area is much less pronounced. In

606   other words, large spots of unexplored voxels in top-canopy affected almost randomly both empty and

607   dense above volumes (**Fig. 4**). As a result, such strong exposure to occlusion led to underestimations

608   of significant but very heterogeneous magnitudes along vertical profiles (Fig 7B). It suggests that such

609   underestimations depend on both the canopy structure and the degree of occlusion, which are both

610   hardly predictable. On the contrary, coarser voxel sizes were much less affected by occlusion, and

611   were rather affected by a significant but spatially homogenous negative bias attributed to clumping

612   effect. In these conditions, it seems a better strategy to avoid erratic negative biases resulting from the

613   strong occlusion inherent to small voxel size by using coarser voxel sizes corrected for a more

614   constant and measurable bias and less prone to large occlusion spots.

615   However, independently of the voxel size, such a negative bias is expected to systematically

616   occur in layers where occlusion starts, as soon as the dense voxels are clumped. Thus the "mean layer"

617   method for dealing with unsampled voxels is not satisfying. Additionally, it raises sharp errors locally.

618   Strong underestimations at layer and plot scales are in accordance with previous observations

619   from ground perspectives (Schneider et al., 2019). Increasing the number of scans and the voxel size

620   limited occurrence of unexplored voxels, so that estimations were generally improved. However,

621   highest number of scans with smallest voxel size or single scan with 0.5 m voxel size were still

622   affected. Hence, the appropriate combination of scan design and voxel size directly depends of the

623   vegetation density and of the level of detail required to match user's aim. Typically, retrieving LAD

624   profiles shapes and values with 20% error can be achieved either by 5 scans with 0.1 m voxels or by a

625   single scan with 0.5 m voxels in sparse vegetation structures **(Fig 8AB)**. However, in dense vegetation

626   and/or when estimates at voxel scale are valuable (i.e. for 3D radiative transfer modelling), it seems

627   mandatory to rely on both multiple viewpoints and coarse voxels to retrieve unbiased estimates and

628   reliable voxel LAD value (**Fig. 8CD**). Similarly to (Schneider et al., 2019), until 80% of voxels can be

629   occluded in critical cases **(Fig. 8EF)**.

630   By calculating confidence intervals at voxel scale, our study gives insights on the drop in local

631   accuracy within voxel resulting from poor sampling conditions. This differs from the usual approach

for quantifying occlusion consisting in counting voxel with at least one beam passing through, thus ignoring errors generated in poorly sampled voxels. Confidence intervals indicated that estimations in poorly sampled voxel can be affected by 1 m^{-1} errors, which is considerable regarding the range of reference LAD values. These confidence intervals can be considered as a statistical alternative to the use of mean nearest neighbour point (Wilkes et al., 2017) in order to assess the sampling densities of given areas, in particular when used approaches are sensitive to non-uniform distribution of points (i.e. for geometrical modelling of trees). Small voxels were frequently affected by large errors, until 35% of the scene. With the 4-5 scans design with 0.1 m voxels, CI > 1 m^{-1} are even more frequent than with a single scan (**Fig 8E**). This higher frequency of large CI was due to the poor exploration of voxels which would have remained unexplored with a single scan, producing unreliable estimates. Locally, such errors were worse than replacing estimates by the mean layer value, suggesting that the reduction of occluded voxel percentage should not be the single criteria for sampling accuracy, and raised the question of the appropriate criterion for occlusion. Determining whether to replace voxel by a fixed value or to keep the estimation given by few beams is particularly difficult in clumped situations given the strong correlation observed between occlusion areas and high LAD values areas. This advocates for the development of correction techniques that are not based on numerical thresholds (Soma et al. 2020).

4.3. Recommendations and research needs

All identified estimation biases were negative. The vegetation heterogeneity effect could yield up to 20% underestimations (**Fig. 6**, **Fig. 7BD**), while unsampled voxels led to profiles that could be locally less than half of reference (**Fig. 8A**), and even worst locally. In the field, these negative biases are entangled and add up, which can potentially induce a global stronger bias than observed in these simulations. Hence, these biases should not be overlooked and we strongly recommend to limit their magnitude and correct them when possible. This study confirms observations of Béland et al., 2014a at the scale of individual trees, i.e. increasing voxel size is an efficient way to level up sampling at voxel scale. Such coarser discretization level should be considered with caution, as it leads to the

660   aggregation of gaps and clumps, as well as the aggregation of occluded and explored areas in same

661   voxels. However, negative bias resulting from occurrence of occlusion are unstable and of higher

662   magnitude and should be avoided in first place, suggesting coarse voxel sizes remain an advantageous

663   option. To determine the appropriate voxel size, the ability to correct for subgrid vegetation

664   heterogeneity (Soma et al., 2018) and to assess accuracy with confidence intervals are key steps.

665   In light of our results, we recommend to use unbiased estimators and to rely on multiple

666   viewpoints. Tested vegetation scene had a 10 m extent in each dimension, with no or few vegetation

667   below 3 m height. The density of scans was relatively high (2.5 m between scans) compared to other

668   studies (Schneider et al., 2019; Wilkes et al., 2017). However, the simulated vegetation features,

669   which were representative of Mediterranean canopies (Simioni et al., 2016), displayed much denser

670   clumps of LAD values (0.6 m^{-1} in average) compared to retrieved LAD in other vegetation types

671   ($\sim$ 0.3 m^{-1}). In such dense context, occlusion occurred from 5 m height, while accurate sampling has

672   been observed until 35-m height with multi-echoes instrument and in other field conditions (Schneider

673   et al., 2019). This proves that *a priori* recommendations concerning visibility analysis can hardly be

674   applied to a range of vegetation structures and different forest types. Providing exhaustive guidelines

675   based on easily measurable stand parameters, i.e. number of large stems (Abegg et al., 2017), presence

676   of understorey or mean crown width could help to plan appropriate scan design across sites.

677   Additionally, the terrestrial LiDAR simulated in this study was a single echo scanner, typically

678   representative of the FARO Focus 3D, which is used in operational context for French forest

679   monitoring. Other scanners, such as RIEGL VZ400, a multi-echoes LiDAR, have better exploration

680   skills and are less sensitive to occlusion. Then, as suggested in (Wilkes et al., 2017), recommendations

681   should also be adapted to the type and resolution of instruments. Yet, beam density also decreases at a

682   given distance of these multi-echoes instruments, so that such scanners are theoretically exposed to the

683   same bias arising from occlusion, as confirmed by observations in tropical canopies (Schneider et al.,

684   2019). The bias arising from subgrid vegetation heterogeneity is independent of sampling accuracy

685   and, as a result, concerns all instruments. The presence of vegetation in the lower part of the canopy

686   (understorey) might generate more occlusion, requiring to increase the number of scans. Hence, a

687   particular attention should be paid to set instrument in order to obtain viewpoints that enable to

688   efficient plot sampling, for example in open locations (Wilkes et al., 2017). Since the number of scans

689   can generally not be increased in field conditions, a trade off on voxel size must be found. Therefore,

690   we recommend to use medium voxel size, typically close to 0.5 m, with an empirical correction to

691   account for vegetation heterogeneity in the subgrid volume. Scanning from the above perspective (i.e.

692   UAV LiDAR) can provide significant reduction of occluded areas close to tops of canopies, but

693   suffered from a limited penetration of beams in the mid-crown (Morsdorf et al., 2018; Schneider et al.,

694   2019), so that similar negative biases associated with unsampled voxels and subgrid vegetation

695   heterogeneity as identified in the present study should exist.

696   In the present study, we used the mean layer assumption (replacing unsampled voxels by the

697   mean of LAD estimates obtained at corresponding layer) to extrapolate missing data. Such method is

698   theoretically similar to ignoring these missing values in spatial averages, and suffer from strong local

699   inaccuracy in dense or empty areas differing from mean LAD value. Additionally, poorly sampled

700   voxels had frequent unreliable estimates, which might be locally more erroneous than replacing by the

701   biased mean layer value. First, it shows the benefit of quantifying uncertainties of estimations in

702   locations of interests (i.e. dense voxels), which should be included in further analysis when estimating

703   LAD. Second, it raises the question of the definition of an occluded voxel.

704   In our numerical experiment, the leaf orientation factor, the leaf fraction, and the distance

705   effect were known and corrected so that our estimators of the LAD were unbiased in each voxel to

706   limit confounding errors in the numerical experiment. However, such parameters are challenging to

707   retrieve in field conditions and their estimations are expected to induce errors (Yan et al., 2019), which

708   might affect the outcome of the present study. The leaf orientation factor can be for example retrieved

709   by leaves triangulations if LiDAR resolution is fine enough (Bailey and Mahaffee, 2017). Several

710   classification methods have been proposed to classify leaves *versus* wood hits (Wang et al., 2020).

711   Then, the leaf fraction factor can be retrieved as the ratio between leaves and total number of points in

712   a given voxel. Eventually, the effect of the distance to scanner can be either estimated from laboratory

713   experiments (Soma et al. 2018) or physical modelling of beam divergence (Béland et al., 2011). The

714   occlusion bias highlighted in the present work should also be explored in other vegetation scenes with

715   absolute references, e.g. with point clouds arising from the sampling of 3D tree models. We showed

716   that underestimations constantly affected dense voxels where occlusion begin, but that voxels can be

717   affected independently of their vegetation density in background and/or top layers, including empty

718   areas. The consequences of this sampling bias in those partially explored layers directly depend on the

719   representativeness of remaining sampled voxels, which can either results in top profile

720   overestimations, underestimations or even in a limited bias. Then, we recommend to analyse the

721   magnitude of this bias for a variety of vegetation structures in light of optical depth and correlation

722   length in vegetation (Appendix B). This variability in spatial bias distribution, vegetation structure and

723   the difficulty to define an occluded volume demonstrate the need for spatially adaptive methods to

724   deal both with poorly sampled and fully occluded voxels. Given the clumped structure of vegetation,

725   using the information of surrounding voxels is a promising approach. Such method relying on kriging

726   has been developed and tested both on a virtual scene (e.g. in Appendix B), and then applied to field

727   data (Soma et al., 2020). Corrections yielded encouraging results with a buffering of errors due to

728   sampling limitations and a more adaptive guess of unexplored voxels values, holding the potential to

729   retrieve better voxel and plot LAD estimations.

730   **5. Conclusion**

731

732   The present work disentangles some of biases related to LAD estimations with TLS through a

733   numerical study. This simulation framework was mandatory to fully understand and quantify the

734   magnitude of these major biases, because they mainly occur in dense and clumped canopy context, for

735   which field references are often not available. Moreover, such a design allows vegetation

736   manipulation, such as smoothing to ease analysis. First, simulations allowed to characterize a negative

737   bias for LAD estimation due to subgrid vegetation heterogeneity in voxels, arising from dense and

738   light density areas being encompassed within same volumes. Second, we assessed sampling accuracy

739   with confidence intervals and identified a spatial correlation between occlusion and dense LAD in

740   layers where occlusion of the laser beams starts to occur. This spatial correlation leads to

741   underestimation of LAD profile, even when the mean layer value was attributed to unsampled voxels.

742   Several methods to limit occurrence of unsampled voxels and increase sampling rate were efficient to

743 damper underestimations. We confirm that combining the information from several scan positions was

744 critical to improve the reliability of estimates. Moreover, the negative bias arising from unsampled

745 voxels was prone to large and unstable variations of magnitude depending on the canopy structure.

746 Then, we recommend to solve in first place the occurrence of unsampled areas, typically by using

747 estimations from coarse voxels complemented by an adequate treatment of subgrid vegetation

748 heterogeneity effect. In the present study, we found that at least 0.5 m voxel size was appropriate, with

749 a mandatory correction for vegetation heterogeneity. The development of methods to extrapolate or

750 correct LAD values in occluded volumes (e.g. kriging) remains a challenging but critical need. The

751 simulation framework developed in our study cannot serve as sole reference for quantifying the

752 magnitude of similar biases occurring with the diversity of natural vegetation and acquisition

753 parameters, as many uncertainties that are inherent to the field conditions are neglected in numerical

754 experiments. Yet, this study paves the way for additional research and field measures needed to

755 characterize in operational context the biases identified in these simulations.

756

757 **Author Contributions**

758 M.S. conceived and designed the experiments; M.S. performed the experiments, as well as the

759 analyses, with useful guidelines of F.P. and J-L.D. . M.S. wrote the paper, with critical contributions

760 of the other co-authors.

761

766

767 **6.   References**

768 Abegg, M., Kükenbrink, D., Zell, J., Schaepman, M.E., Morsdorf, F., 2017. Terrestrial laser

769   scanning for forest inventories-tree diameter distribution and scanner location impact on

770   occlusion. Forests 8. https://doi.org/10.3390/f8060184

771   Bailey, B.N., Mahaffee, W.F., 2017. Rapid measurement of the three-dimensional distribution

772   of leaf orientation and the leaf angle probability density function using terrestrial LiDAR

773   scanning. Remote Sens. Environ. 194, 63–76. https://doi.org/10.1016/j.rse.2017.03.011

774   Béland, M., Baldocchi, D.D., Widlowski, J.L., Fournier, R.A., Verstraete, M.M., 2014a. On

775   seeing the wood from the leaves and the role of voxel size in determining leaf area

776   distribution of forests with terrestrial LiDAR. Agric. For. Meteorol. 184, 82–97.

777   https://doi.org/10.1016/j.agrformet.2013.09.005

778   Béland, M., Widlowski, J.L., Fournier, R.A., 2014b. A model for deriving voxel-level tree

779   leaf area density estimates from ground-based LiDAR. Environ. Model. Softw. 51, 184–

780   189. https://doi.org/10.1016/j.envsoft.2013.09.034

781   Béland, M., Widlowski, J.L., Fournier, R.A., Cote, J.F., Verstraete, M.M., 2011. Estimating

782   leaf area distribution in savanna trees from terrestrial LiDAR measurements. Agric. For.

783   Meteorol. 151, 1252–1266. https://doi.org/10.1016/j.agrformet.2011.05.004

784   Cifuentes, R., Van der Zande, D., Farifteh, J., Salas, C., Coppin, P., 2014. Effects of voxel

785   size and sampling setup on the estimation of forest canopy gap fraction from terrestrial

786   laser scanning data. Agric. For. Meteorol. 194, 230–240.

787   https://doi.org/10.1016/j.agrformet.2014.04.013

788   Côté, J.F., Fournier, R.A., Egli, R., 2011. An architectural model of trees to estimate forest

789   structural attributes using terrestrial LiDAR. Environ. Model. Softw. 26, 761–777.

790   https://doi.org/10.1016/j.envsoft.2010.12.008

791   Durrieu, S., Allouis, T., Fournier, R., Véga, C., Albrech, L., 2008. Spatial quantification of

792   vegetation density from terrestrial laser scanner data for characterization of 3D forest

793   structure at plot level, in: SilviLaser 2008. pp. 325–334.

794   Gollob, C., Ritter, T., Wassermann, C., Nothdurft, A., 2019. Influence of scanner position and

795   plot size on the accuracy of tree detection and diameter estimation using terrestrial laser

796   scanning on forest inventory plots. Remote Sens. 11, 1–30.

797   https://doi.org/10.3390/rs11131602

798 Grau, E., Durrieu, S., Fournier, R., Gastellu-etchegorry, J., Yin, T., 2017. Estimation of 3D

799   vegetation density with Terrestrial Laser Scanning data using voxels . A sensitivity

800   analysis of influencing parameters. Remote Sens. Environ. 191, 373–388.

801   https://doi.org/10.1016/j.rse.2017.01.032

802 Hosoi, F., Nakai, Y., Omasa, K., 2010. Estimation and error analysis of woody canopy leaf

803   area density profiles using 3-d airborne and ground-based scanning lidar remote-sensing

804   techniques. IEEE Trans. Geosci. Remote Sens. 48, 2215–2223.

805   https://doi.org/10.1109/TGRS.2009.2038372

806 Hosoi, F., Omasa, K., 2006. Voxel-based 3-D modeling of individual trees for estimating leaf

807   area density using high-resolution portable scanning lidar. IEEE Trans. Geosci. Remote

808   Sens. 44, 3610–3618. https://doi.org/10.1109/TGRS.2006.881743

809 Hu, R., Bournez, E., Cheng, S., Jiang, H., Nerry, F., Landes, T., Saudreau, M., Kastendeuch,

810   P., Najjar, G., Colin, J., Yan, G., 2018. Estimating the leaf area of an individual tree in

811   urban areas using terrestrial laser scanner and path length distribution model. ISPRS J.

812   Photogramm. Remote Sens. 144, 357–368.

813   https://doi.org/10.1016/j.isprsjprs.2018.07.015

814 Huang, P., Pretzsch, H., 2010. Using terrestrial laser scanner for estimating leaf areas of

815   individual trees in a conifer forest. Trees - Struct. Funct. 24, 609–619.

816   https://doi.org/10.1007/s00468-010-0431-z

817 Kamoske, A.G., Dahlin, K.M., Stark, S.C., Serbin, S.P., 2019. Leaf area density from airborne

818   LiDAR: Comparing sensors and resolutions in a temperate broadleaf forest ecosystem.

819   For. Ecol. Manage. 433, 364–375.

820   https://doi.org/https://doi.org/10.1016/j.foreco.2018.11.017

821   Li, Y., Guo, Q., Tao, S., Zheng, G., Zhao, K., Xue, B., Su, Y., 2016. Derivation, Validation,

822   and Sensitivity Analysis of Terrestrial Laser Scanning-Based Leaf Area Index. Can. J.

823   Remote Sens. 42, 719–729. https://doi.org/10.1080/07038992.2016.1220829

824   Morsdorf, F., Kükenbrink, D., Schneider, F.D., Abegg, M., Schaepman, M.E., 2018. Close-

825   range laser scanning in forests: Towards physically based semantics across scales.

826   Interface Focus 8. https://doi.org/10.1098/rsfs.2017.0046

827   Norman, J.M., Campbell, G.S., 1989. Canopy structure, in: Pearcy, R.W., Ehleringer, J.R.,

828   Mooney, H.A., Rundel, P.W. (Eds.), Plant Physiological Ecology: Field Methods and

829   Instrumentation. Springer Netherlands, Dordrecht, pp. 301–325.

830   https://doi.org/10.1007/978-94-009-2221-1_14

831   Pimont, F., Allard, D., Soma, M., Dupuy, J.-L.J.-L., 2018. Estimators and confidence

832   intervals for plant area density at voxel scale with T-LiDAR. Remote Sens. Environ.

833   215, 343–370. https://doi.org/10.1016/j.rse.2018.06.024

834   Pimont, F., Dupuy, J.L., Caraglio, Y., Morvan, D., 2009. Effect of vegetation heterogeneity

835   on radiative transfer in forest fires. Int. J. Wildl. Fire 18, 536–553.

836   https://doi.org/10.1071/WF07115

837   Pimont, F., Soma, M., Dupuy, J.-L., 2019. Accounting for Wood, Foliage Properties, and

838   Laser Effective Footprint in Estimations of Leaf Area Density from Multiview-LiDAR

839   Data. Remote Sens. 11, 1580. https://doi.org/10.3390/rs11131580

840   Pimont, F., Soma, M., Dupuy, J.-L., Rigolot, E., Jean, F., 2016. Estimating canopy load and

841   bulk density distribution using calibrated T-LiDAR indices, in: Proceedings for the 5th

842   International Fire Behavior and Fuels Conference. International Association of Wildland

843   Fire, Missoula, Montana, USA, Portland, Oregon, USA, pp. 3–8.

844   Ruel, J.J., Ayres, M.P., 1999. Jensen ' s inequality predicts effects of environmental variation.

845   Tree 5347, 361–366. https://doi.org/10.1016/S0169-5347(99)01664-X

846   Schlather, M., Malinowski, A., Menck, P.J., Oesting, M., Strokorb, K., 2015. Analysis,

847   Simulation and Prediction of Multivariate Random Fields with Package RandomFields.

848   J. Stat. Softw. 63. https://doi.org/10.18637/jss.v063.i08

849   Schneider, F.D., Kükenbrink, D., Schaepman, M.E., Schimel, D.S., Morsdorf, F., 2019.

850   Quantifying 3D structure and occlusion in dense tropical and temperate forests using

851   close-range LiDAR. Agric. For. Meteorol. 268, 249–257.

852   https://doi.org/10.1016/j.agrformet.2019.01.033

853   Simioni, G., Marie, G., Huc, R., 2016. Influence of vegetation spatial structure on growth and

854   water fluxes of a mixed forest: Results from the NOTG 3D model. Ecol. Modell. 328,

855   119–135. https://doi.org/10.1016/j.ecolmodel.2016.02.004

856   Soma, M., Pimont, F., Allard, D., Fournier, R., Dupuy, J.-L., 2020. Mitigating occlusion

857   effects in Leaf Area Density estimates from Terrestrial LiDAR through a specific kriging

858   method. Remote Sens. Environ. 245, 111836. https://doi.org/10.1016/j.rse.2020.111836

859   Soma, M., Pimont, F., Durrieu, S., Dupuy, J.-L.J.-L., 2018. Enhanced Measurements of Leaf

860   Area Density with T-LiDAR: Evaluating and Calibrating the Effects of Vegetation

861   Heterogeneity and Scanner Properties. Remote Sens. 10, 1580.

862   https://doi.org/10.3390/rs10101580

863   Stark, S.C., Leitold, V., Wu, J.L., Hunter, M.O., de Castilho, C. V, Costa, F.R.C., McMahon,

864   S.M., Parker, G.G., Shimabukuro, M.T., Lefsky, M.A., Keller, M., Alves, L.F., Schietti,

865   J., Shimabukuro, Y.E., Brandão, D.O., Woodcock, T.K., Higuchi, N., de Camargo, P.B.,

866   de Oliveira, R.C., Saleska, S.R., 2012. Amazon forest carbon dynamics predicted by

867   profiles of canopy leaf area and light environment. Ecol. Lett. 15, 1406–1414.

868   https://doi.org/10.1111/j.1461-0248.2012.01864.x

869   Wang, D., Momo Takoudjou, S., Casella, E., 2020. LeWoS: A universal leaf-wood

870   classification method to facilitate the 3D modelling of large tropical trees using

871   terrestrial LiDAR. Methods Ecol. Evol. 11, 376–389. https://doi.org/10.1111/2041-

872   210X.13342

873   Weiss, M., Baret, F., Smith, G.J., Jonckheere, I., Coppin, P., 2004. Review of methods for in

874   situ leaf area index (LAI) determination Part II. Estimation of LAI, errors and sampling.

875   Agric. For. Meteorol. 121, 37–53. https://doi.org/10.1016/j.agrformet.2003.08.001

876   Wilkes, P., Lau, A., Disney, M., Calders, K., Burt, A., Gonzalez de Tanago, J., Bartholomeus,

877   H., Brede, B., Herold, M., 2017. Data acquisition considerations for Terrestrial Laser

878   Scanning of forest plots. Remote Sens. Environ. 196, 140–153.

879   https://doi.org/10.1016/j.rse.2017.04.030

880   Yan, G., Hu, R., Luo, J., Weiss, M., Jiang, H., Mu, X., Xie, D., Zhang, W., 2019. Review of

881   indirect optical measurements of leaf area index: Recent advances, challenges, and

882   perspectives. Agric. For. Meteorol. 265, 390–411.

883   https://doi.org/10.1016/j.agrformet.2018.11.033

884   Yun, T., Cao, L., An, F., Chen, B., Xue, L., Li, W., Pincebourde, S., Smith, M.J., Eichhorn,

885   M.P., 2019. Simulation of multi-platform LiDAR for assessing total leaf area in tree

886   crowns. Agric. For. Meteorol. 276–277, 107610.

887   https://doi.org/10.1016/j.agrformet.2019.06.009

888   Zhao, K., García, M., Liu, S., Guo, Q., Chen, G., Zhang, X., Zhou, Y., Meng, X., 2015.

889   Terrestrial lidar remote sensing of forests: Maximum likelihood estimates of canopy

890   profile, leaf area index, and leaf angle distribution. Agric. For. Meteorol. 209–210, 100–
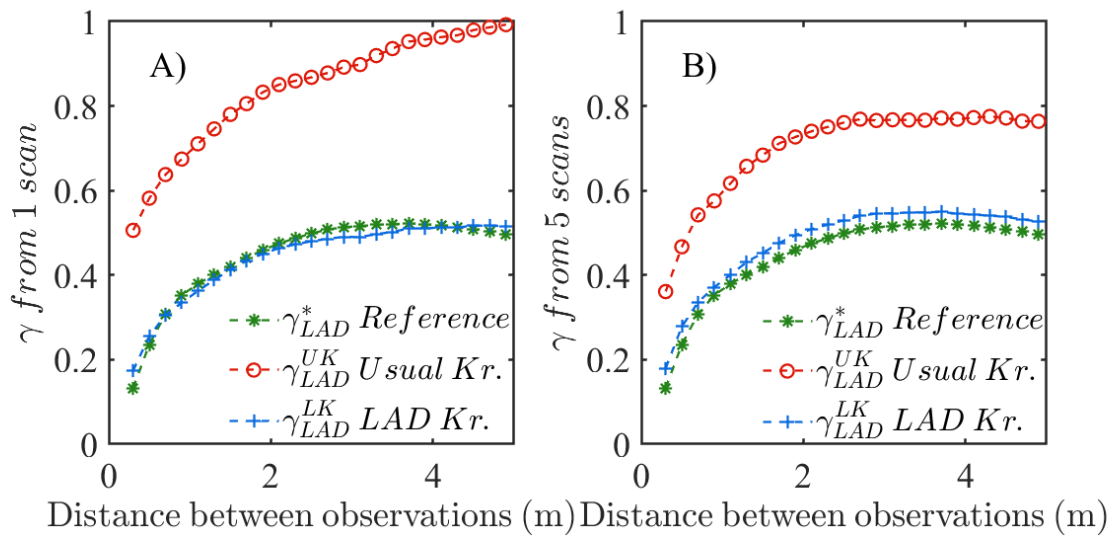
891   113. https://doi.org/10.1016/j.agrformet.2015.03.008

892

893   **Appendix A**

894
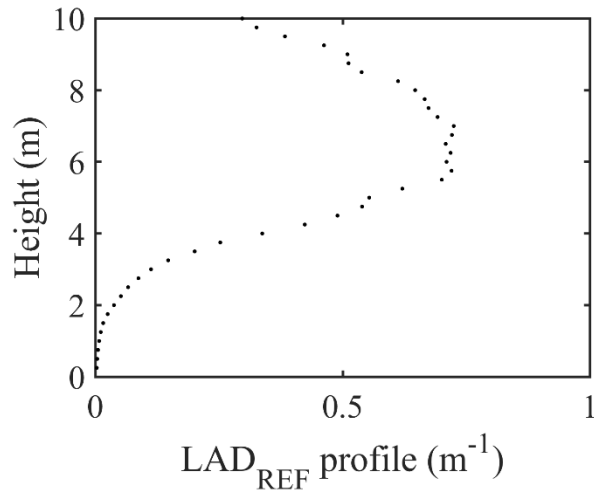
A1. Vertical profile of simulated reference Leaf Area Density 3D field.

Appendix B

897

B1. Variogram of the reference vegetation scene (green crosses). Estimated variograms from

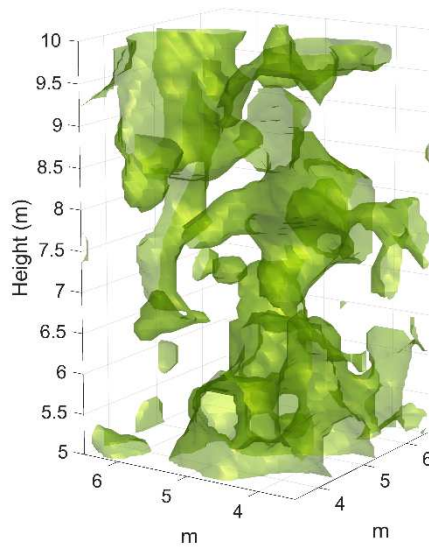$\widehat{LAD}$ computed for usual kriging method (red circle) and with the kriging method specific to LAD

(blue cross) for the scan design corresponding to A) Single viewpoint; B) Five viewpoints. For more

details, please refers to Soma et al. 2020.

Appendix C

904

905   C1. Isosurface of the simulated vegetation scene from RandomFields package. To ease visualization,

906   only a subsample of the scene is displayed (core of the plot).

907

908   **Appendix D**

909   We assessed the significance of voxel size and number on scans effects on estimations though

910   a statistical analysis. Voxels resulting from the fine and coarse discretization levels of the

911   vegetation scene cannot be considered as independent observations when comparing voxel

912   sizes, as voxels share the same vegetation in occupied volumes, with respect to their size (e.g.

913   several 0.1 m voxels are contained in the 0.5 m voxel at the same location). To account for

914   such specificity, all estimations were smoothed to the largest voxel size voxels, i.e. 1 m, and

915   tests were performed at this scale. Smoothing was done by averaging 0.1 m – 0.2 m and 0.5 m

916   voxels with respects to the 1 m voxel size grid. As voxels arise from the same vegetation

917   scene, observations (voxels) cannot be considered independent between treatments (voxel size

918   * number of scans), but should be considered as a repeated measure on the same individual.

919   Hence, we performed a two-way ANOVA with repeated measures using R software (R Core

920   Team (2016). R: A language and environment for statistical computing. R Foundation for

921   Statistical Computing, Vienna, Austria. URL https://www.R-project.org/). The analysis was

922   carried out with estimation errors $(LAD_{REF,i} - \widehat{LAD_i})$ as predictor, for the 0.1 m, 0.2 m, 0.5 m

923   and 1 m voxel sizes and for the two scans and five scans designs :

924    $$(LAD_{REF,i} - \widehat{LAD_i}) \sim IDvox / (Voxel\ size + Number\ of\ scans)$$

925   with *IDvox* the voxel ID used for the within-subject model computation.

Effects	D.F.	F-value	P-Value
IDvox	999	-	-
IDvox : Voxel size	3	27.1	2e-16 ***
IDvox : Number of scans	1	34.31	6.4e-9 ***

926

927   In accordance with graphical observations, both effects of voxel size and of number of scans

928   are significant on the error in estimation of LAD value.